

1 **Probing cellular response to topography in three dimensions**

2 Colin D. Paul, Alex Hruska, Jack R. Staunton, Hannah A. Burr, Kathryn M. Daly, Jiyun Kim,

3 Nancy Jiang, and Kandice Tanner*

4

5

6

7

8

9

10

11

12

13 Laboratory of Cell Biology, Center for Cancer Research, National Cancer Institute, National

14 Institutes of Health

15 * Corresponding author information: Dr. Kandice Tanner; Center for Cancer Research, National

16 Cancer Institute, Building 37, Room 2132, Bethesda, MD 20892; Ph: 260-760-6882; Email:

17 kandice.tanner@nih.gov

18

19 **ABSTRACT (275/300)**

20 Biophysical aspects of in vivo tissue microenvironments include microscale mechanical
21 properties, fibrillar alignment, and architecture or topography of the extracellular matrix (ECM).
22 These aspects act in concert with chemical signals from a myriad of diverse ECM proteins to
23 provide cues that drive cellular responses. Here, we used a bottom-up approach to build fibrillar
24 architecture into 3D amorphous hydrogels using magnetic-field driven assembly of paramagnetic
25 colloidal particles functionalized with three types of human ECM proteins found in vivo. We
26 investigated if cells cultured in matrices comprised of fibrils of the same size and arranged in
27 similar geometries will show similar behavior for each of the ECM proteins tested. We were able
28 to resolve spatial heterogeneities in microscale mechanical properties near aligned fibers that were
29 not observed in bulk tissue mechanics. We then used this platform to examine factors contributing
30 to cell alignment in response to topographical cues in 3D laminin-rich matrices. Multiple human
31 cell lines extended protrusions preferentially in directions parallel or perpendicular to aligned
32 fibers independently of the ECM coating. Focal adhesion proteins, as measured by paxillin
33 localization, were mainly diffuse in the cytoplasm, with few puncta localized at the protrusions.
34 Integrin $\beta 1$ and fascin regulated protrusion extension but not protrusion alignment. Myosin II
35 inhibition did not reduce observed protrusion length. Instead, cells with reduced myosin II activity
36 generated protrusions in random orientations when cultured in hydrogels with aligned fibers.
37 Similarly, myosin II dependence was observed in vivo, where cells no longer aligned along the
38 abluminal surfaces of blood vessels upon treatment with blebbistatin. These data suggest that
39 myosin II can regulate sensing of topography in 3D engineered matrices for both normal and
40 transformed cells.

41

42

43 **KEYWORDS:** Topographical cues; engineered matrices; microrheology; physical properties; cell

44 alignment; cell protrusions

45

46 INTRODUCTION

47 The physical properties of the extracellular matrix (ECM) milieu are widely acknowledged
48 as fundamental determinants of cell fate, tissue homeostasis, immune response, wound healing,
49 and cancer progression [1-4]. Within a given tissue, the ECM not only provides structural support
50 but regulates cell signaling via reciprocal biochemical and biophysical cues [5]. On one hand, the
51 ECM contributes to overall tissue mechanics, and the effects of mechanical properties on cell fate
52 and phenotype have been extensively studied using in vitro and in vivo assays [6-15]. For example,
53 tissues become progressively stiffer as a function of malignant transformation from normal to
54 tumors [9]. In addition, the architecture of the ECM provides structural feedback, such as
55 topographical cues [13-16]. Topography, simply described, refers to the shape and profile of a
56 given material's surface [17-19]. Cells respond to topographical and stiffness-mediated cues
57 through biochemical signaling via cellular adhesions and cytoskeletal attachments to the ECM
58 [20]. Cell sensing of architectural and mechanical cues is a complex phenomenon where ECM
59 adhesion molecules act concomitantly with intracellular machinery to drive cellular responses
60 [21]. In vivo, tissue topographical cues are heterogeneous, with hybrid structures comprised of
61 aligned ridges and pores that span lengths from nanoscale to microscale [17-19]. On the nanoscale
62 level, ECM proteins can adopt different morphologies, such as globular and fibrillar architectures
63 [17, 18]. One such example is fibronectin (FN), which presents different cell binding sites and is
64 alternatively spliced to generate conformation which initiate distinct signaling cascades [22, 23].
65 On the other hand, the chemical specificity of these building blocks in turn also regulate unique
66 signaling cascades. For example, cells that interact with fibronectin fibrils receive distinct
67 chemical cues from those received when exposed to cues derived from collagen type I fibrils. Yet,
68 in some cases, physical cues may dominate cellular response in the presence of a chemical cue.
69 Simulations of stretching of a module of a FN fibril, FN III, is sufficient to override beta one-

70 dependent modulation of increased ligand binding and associated down-stream signaling. Thus,
71 understanding how cells “sense” these interconnected cues and how they influence eventual cell
72 fate remains a perplexing issue.

73 These concepts are often difficult to discern using naturally derived 3D tissue mimetics, as
74 precise control of ligand density and architecture are often intertwined. Moreover, dissecting
75 differential physical cues such as mechanics from architecture is also challenging. While studies
76 using patterned two-dimensional substrates [24, 25] and microfabricated environments [26] have
77 revealed aspects of cell response to topography, reactions to topographic cues in more
78 physiologically relevant three-dimensional environments are not as well understood. Importantly,
79 three-dimensional cues are likely vital to recapitulate some aspects of physiological
80 mechanosensing. Also, cell attachments to matrices in 3D environments often differ with respect
81 to that observed for cells cultured in 2D substrates, which in turn may impact mechanosensing in
82 specific 3D ECMs. In tissue, 3D topographies consist of highly oriented structures that are not
83 well-recapitulated by *in vitro* hydrogel models. For example, commonly used collagen hydrogels
84 form fibers that are randomly oriented unless some external micropatterning is imposed during
85 their polymerization [27]. Similarly, laminin-rich ECMs (Matrigel) form amorphous gels devoid
86 of cell-scale structures [28]. To address the need for reproducible 3D culture systems with well-
87 defined matrix architecture and ECM protein composition, we recently developed a method
88 whereby functionalized paramagnetic colloidal particles are magnetically aligned in 3D hydrogels
89 to create fibrils that span microns in length and 10s of nms in widths [17, 29]. Fiber alignment,
90 diameter, spacing, and extracellular matrix conjugation to the colloidal particles can be controlled
91 to create defined topography independently of the ligand used to coat the particles. In 3D Matrigel
92 matrices containing aligned particles, mouse fibroblasts and neural cell lines send out protrusions

93 that are longer than those seen in matrices lacking particle alignment, independently of the ECM
94 ligand conjugated to the colloidal particles. When the particles are coated in fibronectin, these cells
95 preferentially extend protrusions either parallel or perpendicular to the fibers. This system allows
96 us to test if cells cultured in matrices where fibrils of the same size and arranged in similar
97 geometries will show similar behavior for different types of ECM proteins. In this system, the bulk
98 mechanical properties were similar regardless of the presence of aligned or unaligned colloidal
99 particles. However, lack of understanding of mechanical cues at the cellular scale, of how ECM
100 nanoparticle conjugation affects cell response, and of mechanistic factors driving cell response to
101 topography limited the use of this system.

102 Here, we used our system to discern the role of aligned topographical cues, presented
103 across a range of human ECM proteins, on human cell response in Matrigel (laminin-rich) matrices
104 with well-characterized physical properties. Using optical trap-based active microrheology, we
105 measured the 3D microscale viscoelasticity. We then asked how topographical and
106 micromechanical cues influence human normal (human foreskin fibroblast, HFF) and cancer (U87
107 glioblastoma) cells on this length scale. Using genetic manipulation and small molecule inhibitors,
108 we determined that β 1 integrin and fascin reduced the length of cell protrusions in response to
109 physical cues resulting from fiber alignment in these engineered Matrigel matrices. However,
110 protrusions were still aligned with the fibrils. In contrast, reduced myosin II activity did not affect
111 protrusion length, but protrusions were randomly oriented. We confirmed that myosin II is also
112 required by cells to sense topographical alignment in vivo using the zebrafish brain vasculature as
113 our model system. Our results suggest that normal and cancer cells use similar machinery to
114 respond to the topographical and micromechanical cues in this system, where myosin II may
115 regulate how cells sense topographical cues.

116

117 **MATERIALS AND METHODS**

118 **Cell culture**

119 Human foreskin fibroblast cells were cultured in Dulbecco's Modified Eagles Medium
120 (DMEM) supplemented with 10% fetal bovine serum, 1% penicillin-streptomycin, and 1% L-
121 glutamine and maintained at 37°C and 10% CO₂. Human U87 glioma cells were cultured in the
122 same medium but maintained at 37°C and 5% CO₂. Cells were sub-passaged every 2-3 days.

123 **Conjugation of fluorophores to human proteins**

124 We employed several proteins. Human laminin (pepsinized; Millipore Sigma, Burlington,
125 MA, Catalog #AG56P), human tenascin-C (Millipore Sigma, Catalog #CC065), and human
126 plasma fibronectin (Millipore Sigma, Catalog #FC010) were conjugated to fluorophores using the
127 DyLight™ 488 Microscale Labeling Kit (ThermoFisher Scientific, Waltham, MA, Catalog
128 #53025) according to the manufacturer's instructions. Briefly, proteins were supplied in
129 suspension at concentrations ranging from 0.25-1 mg/ml. Laminin and tenascin-C were at
130 concentrations less than recommended for labeling (0.5 mg/ml and 0.25 mg/ml, respectively;
131 suggested concentration for conjugation to fluorophore is 1 mg/ml). For these proteins, 50 µg and
132 25 µg, respectively, were used in the labeling reaction instead of the recommended 100 µg. Bovine
133 serum albumin (BSA) dissolved in PBS at a concentration of 1 mg/ml was also labeled for use as
134 a control that does not specifically bind to cell adhesion proteins. Following labeling, protein
135 concentrations were measured using a DeNovix DS-11+ Spectrophotometer and the "Labeled
136 Protein" module. E1% was set at 10 g/100 ml, 1A = 1 mg/ml, with analysis wavelength for

137 fluorescence at 494 nm, extinction coefficient set at 71,000, A260 factor of 0.3, and A280 factor
138 of 0.11. Successful labeled was indicated by an absorption peak at 494 nm.

139 **Conjugation of proteins to magnetic colloidal particles**

140 Labeled proteins were conjugated to 300-nm diameter paramagnetic colloidal particles as
141 described previously using the Ademtech Carboxy-Adembeads Coupling Kit (Ademtech, Pessac,
142 France, Catalog #02820) [17]. Briefly, 0.5 mg of carboxylated superparamagnetic colloidal
143 particles were washed twice in 100 μ l Activation Buffer before being resuspended in 100 μ l of
144 fresh Activation Buffer. The beads were then activated by the addition of 100 μ l of 4 mg/ml EDC
145 (resuspended in Activation Buffer) to the colloidal particles in solution, and this mixture was
146 incubated for 1 h at room temperature. To conjugate proteins to the beads, 20 μ g of fluorescently-
147 labeled protein in solution was added to the tube, and the mixture was incubated overnight under
148 gentle shaking. Then, 200 μ l of 0.5 mg/ml BSA in Activation Buffer was added to the tube and
149 incubated while shaking for 1 h at room temperature to quench the reaction. Functionalized beads
150 were washed three times with 100 μ l Storage Buffer, and beads were then stored at a final
151 concentration of 10 mg/ml in Storage Buffer at 4°C for up to 2 weeks.

152 **Cell seeding and topographic alignment in 3D matrices**

153 Matrigel (BD Corning, Corning, NY, Catalog #356230) was thawed on ice and maintained
154 at 4°C. Prior to experiments, Matrigel was stored on ice to reach a stable temperature. A 100 μ l
155 aliquot of Matrigel was spread uniformly over the surface of a Lak-Tek 4-well chambered
156 coverglass well (ThermoFisher, Catalog #155383) chilled on ice and placed in an incubator at
157 37°C for 5 minutes to polymerize. Prior to seeding in 3D culture, HFF or U87 cells were washed
158 with phosphate buffered saline (PBS), detached from the cell culture flask using 10 mM EDTA in

159 PBS, washed once in growth medium, centrifuged at 1000 rpm for 5 min, and resuspended to a
160 concentration of 2×10^6 cells/ml in serum-free medium. Cells were then mixed with functionalized
161 colloidal particles and Matrigel in the following ratio: 12 μ l beads at a concentration of 10 mg/ml,
162 430 μ l Matrigel, and 50 μ l cell suspension (100,000 cells).

163 The mixture was gently mixed by pipette and added to a well of the 4-well coverslide. For
164 alignment of the colloidal particles, the slide was immediately placed on a magnet (NdFeB magnet,
165 K&J Magnetics, Pipersville, PA, Catalog #BX8X8X8, 25.4 mm x 25.4 mm x 25.4 mm) chilled in
166 ice for 15 minutes. Following alignment, the slide was placed in the 37°C incubator for 30 minutes
167 to polymerize the Matrigel. For unaligned topographies, slides were placed on ice far from the
168 magnet for 15 minutes following the addition of the cell/nanoparticle/Matrigel mixture and then
169 polymerized for 30 minutes at 37°C. Wells on the slides were seeded sequentially to ensure proper
170 nanoparticle alignment over the center of the magnet, where field lines are parallel. Following
171 Matrigel polymerization, 350 μ l of serum-free medium was added to each well. Slides were placed
172 in the incubator for 24 h prior to fixation. As a control, an equal number of cells was seeded in a
173 Matrigel matrix, where the 12 μ l bead mixture was replaced with pure Matrigel, resulting in a
174 matrix containing cells but no additional ECM-conjugated colloidal particles.

175 To seed cells in aligned and unaligned agarose matrices, a solution of 1% agarose
176 (Millipore Sigma, Catalog #A9414-25G) dissolved in serum free media and sterilized with a 0.22
177 μ m filter was prepared. Chamber slides were coated with 300 μ l/well agarose. The cell solution,
178 particles, and warmed agarose were mixed in the volumes indicated above, and particles were
179 placed on the magnet for alignment (or kept away from the magnet for unaligned matrices) in a
180 40°C incubator for 10 minutes. Slides were then kept at room temperature for 10 minutes for gels

181 to set. A volume of 350 μ l of serum free media was added to the gels, and gels were kept in the
182 incubator for 48 hours prior to fixation and imaging.

183 Hyaluronic acid matrices were prepared using the HyStem Cell Culture Scaffold Kit
184 (Millipore Sigma, Catalog #HYS020). HyStem, Extralink 1, and degassed water were allowed to
185 come to room temperature. Under aseptic conditions, using a syringe and needle, 1.0 ml of
186 degassed water was added to the HyStem bottle containing 10 mg of HyStem, and 0.5 ml degassed
187 water was added to the Extralink 1 bottle containing 5 mg of Extralink. To form the hydrogel, a
188 ratio of one part Extralink to three parts HyStem was used. A 100 μ l aliquot of hydrogel was spread
189 uniformly over the surface of a chamber slide and allowed to polymerize at room temperature for
190 15 minutes. Cells (prepared as described above) were mixed with functionalized nanoparticles and
191 hydrogel in the following ratio: 12 μ l beads at a concentration of 10 mg/ml, 430 μ l HyStem at
192 concentration of 10 mg/ml, 143 μ l of Extralink 1 at a concentration of 0.5 mg/ml, and 50 μ l cell
193 suspension (100,000 cells). The mixture was gently mixed by pipette, and 635 μ l of this mixture
194 was added to a well of the 4-well coverslide. For alignment of the nanoparticles, the slide was
195 immediately placed on the magnet at room temperature for 15 minutes. For unaligned
196 topographies, slides were placed far from the magnet for 15 minutes. Following alignment, the
197 slide was allowed to fully polymerize in the 37°C incubator for 30 minutes. Following hydrogel
198 polymerization, 350 μ l of serum-free medium was added to each well. After 24 h, media was
199 replaced with serum-containing media (10% FBS). Cells were fixed and analyzed 24 h after the
200 media change.

201 **Pharmacological inhibition**

202 Cell contractility was assessed using a myosin II inhibitor (blebbistatin) compared to a
203 vehicle control. For blebbistatin experiments, serum-free media was supplemented with 100 μ M

204 (-)-blebbistatin (Millipore Sigma, Catalog #B0560) or vehicle control (VC; DMSO), and 350 μ l
205 of media was added to embedded cells after matrix topography was set as described above and
206 prior to overnight incubation. Inhibition of fascin was obtained by use of fascin-G2 (Xcessbio, San
207 Diego, CA, Catalog #M60269-2s), where serum-free media was supplemented with 125 μ M of the
208 inhibitor or vehicle control (VC; DMSO), and 350 μ l of media was added to embedded cells after
209 matrix topography was set as described above and prior to overnight incubation. In these
210 experiments, matrices containing fibronectin--conjugated colloidal particles were used. For cells
211 blocked with a function-blocking antibody, cells were resuspended at a concentration of 2×10^6
212 cells/ml in serum-free media containing 30 μ g/ml of an IgG mouse isotype control antibody
213 (abcam, Cambridge, MA, Catalog #ab91353) or a function blocking anti- β 1 integrin antibody
214 (abcam, Catalog #ab24693). Cells were seeded in aligned matrices with fibronectin-conjugated
215 colloidal particles as described above. After matrix topography was set, 350 μ l of serum-free media
216 supplemented with 30 μ g/ml of isotype control or function-blocking antibody was added to each
217 well, and the sample was incubated overnight.

218 **Knockdown of β 1 integrin via siRNA**

219 To knockdown expression of β 1 integrin, cells were detached with 0.25% trypsin-EDTA
220 and plated at 200,000 cells/well in a 6-well plate in 2.5 ml total growth medium. The following
221 day, cells were transfected with ThermoFisher Silencer Select siRNA targeting expression of β 1
222 integrin (ThermoFisher, Catalog #4390824, siRNA ID s7575), or with a negative control (Silencer
223 Select Negative Control No. 1, ThermoFisher, Catalog #4390843). siRNA stored at a
224 concentration of 50 μ M and stored at -20°C and diluted 1:10 in Opti-MEM cell culture medium
225 (ThermoFisher, Catalog #31985070) to reach a concentration of 5 μ M prior to transfection. Per
226 well of a 6-well plate, 3 μ l of siRNA at 5 μ M was mixed with 150 μ l Opti-MEM. In a separate

227 tube, 7.2 μ l RNAiMAX (ThermoFisher, Catalog #13778030) was mixed with 150 μ l Opti-MEM.
228 150 μ l diluted of the Opti-MEM/siRNA mixture was combined with 150 μ l of the Opti-
229 MEM/RNAiMAX mixture and incubated for 5 min at room temperature. To transfect, 250 μ l of
230 this mixture was added to cells plated the previous day, directly to the existing medium. The
231 following day, media was replaced with fresh growth media. After 48 h, cells were prepared for
232 seeding in aligned matrices as described above.

233 To assess knockdown, RNA was isolated from one representative biological replicate of
234 transfected cells using Trizol (ThermoFisher, Catalog #15596018) according to the manufacturer's
235 instructions. Briefly, 0.4 ml Trizol was added directly to cells plated in 6-well plate wells after
236 aspirating media. The lysate was pipetted up and down to homogenize, mixed with 0.2 ml
237 chloroform per ml of Trizol reagent, and centrifuged for 15 minutes at 12,000 x g at 4 °C. The
238 resulting upper aqueous phase containing RNA was mixed with an equal volume of 100% ethanol
239 and processed with the PureLink RNA Mini Kit (ThermoFisher, Catalog #12183020). The mixture
240 was processed through the kit Spin Cartridge by centrifugation at 12,000 x g for 1 minute, washed
241 once with 700 μ l per tube of Wash Buffer I, washed twice with 500 μ l per tube of Wash Buffer II,
242 and eluted in RNase-free water. The resulting RNA concentration was assessed via Nanodrop.

243 cDNA was synthesized using SuperScript IV VILO Master Mix (ThermoFisher, Catalog
244 #11755050). For each sample, 10 μ l of RNA at 100 ng/ μ l was combined with 4 μ l of SuperScript
245 IV VILO Master Mix or No RT Control, and 6 μ l nuclease-free water was added to bring the total
246 volume to 20 μ l. Solutions were gently mixed and incubated at 25°C for 10 minutes, 50°C for 10
247 minutes, and 85°C for 5 minutes.

248 The synthesized cDNA was used for RT-PCR. For each well of a 96-well reaction plate,
249 10 μ l TaqMan Fast Advanced Master Mix (ThermoFisher, Catalog #4444557) was mixed with 2

250 μ l of the synthesized cDNA, 7 μ l nuclease-free water, and 1 μ l of the TaqMan probe. Samples
251 were run in technical triplicates. The FAM-MGB TaqMan probes used were: GAPDH
252 (ThermoFisher, Catalog #4331182, Assay ID Hs04420697_g1) and ITGB1 (ThermoFisher,
253 Catalog #4331182, Assay ID Hs01127536_m1).

254 Gene expression assays were performed on an Applied Biosystems QuantStudio 3
255 (ThermoFisher). Gene expression was normalized to that of GAPDH for each cell type and siRNA
256 status. For cells transfected with siRNA targeting integrin β 1, fold change was calculated from the
257 mean $\Delta\Delta$ C_T of three technical triplicates, as indicated by the manufacturer (Applied Biosystems,
258 “Guide to Performing Relative Quantitation of Gene Expression Using Real-Time Quantitative
259 PCR”). For cells transfected with control siRNA, expression of integrin β 1 was set to 1.

260 **Transduction of paxillin and actin biosensors**

261 HFF cells were plated in 24-well plates the day prior to transduction, with 50,000 cells/well
262 in 1 ml of growth medium. Cells were transduced with a LentiBrite™ paxillin-GFP lentiviral
263 biosensor (Millipore Sigma, Catalog #17-10154) at a MOI of 20 in 1 ml of growth media per well.
264 Transduction media contained 5 μ g/ml polybrene transfection reagent (Millipore Sigma, Catalog
265 #TR-1003-G). After 24 h, transduction media was replaced with fresh growth media. After an
266 additional 24 h incubation, cells were plated in 3D matrices as described above. Cells were
267 concurrently plated on 2D surfaces coated with Matrigel to assess GFP-paxillin expression on
268 surfaces where focal adhesions were expected to form.

269 Similarly, U87 cells were transfected with a LifeAct TagRFP adenoviral vector (rAV-
270 CMV-LifeAct, ibidi, Martinsried, Germany, Catalog #60122). Briefly, 1 million U87 cells were
271 seeded in a T75 flask and infected at a MOI of 15 in 5 ml serum free media containing 26.6 μ l

272 ibiBoost adenovirus transduction enhancer (ibidi, Catalog #50301). Media containing virus was
273 removed and replaced with fresh media after 4 h. Live cells expressing LifeAct were imaged
274 immediately after seeding in 3D Matrigel matrices containing fibronectin-conjugated colloidal
275 particles.

276 **Cell fixation and fluorescent staining**

277 For samples embedded in Matrigel matrices (with or without colloidal particles), media
278 was aspirated, and each well was washed with 200 μ l PBS. To each well, 300 μ l of 4%
279 paraformaldehyde diluted in PBS was added, and samples were incubated for 3 hours at room
280 temperature. Fixed samples were washed three times with 200 μ l/well PBS. Samples were then
281 incubated with 300 μ l/well of 1% BSA in PBS at room temperature for 30 minutes to block non-
282 specific binding and subsequently washed twice with 200 μ l/well PBS. A phalloidin stock solution
283 was prepared by dissolving 10 nmol of phalloidin-Atto 565 (Millipore Sigma, Catalog #94072-
284 10NMOL) in 500 μ l methanol. To fluorescently label F-actin and the nucleus, a solution containing
285 2 μ g/ml Hoechst 33258 (ThermoFisher, Catalog #H3569) and 30 μ l phalloidin stock/ml in 1%
286 BSA in PBS was prepared. Cells were stained with 200 μ l/well of the staining solution at room
287 temperature for 3 h, then washed three times with 200 μ l/well PBS. Samples were stored in PBS
288 at 4°C prior to imaging. Cells transduced with the GFP-paxillin biosensor were prepared following
289 the same procedure, but the actin cytoskeleton was stained with a 1:40 dilution of AlexaFluor™
290 633 phalloidin (ThermoFisher, Catalog #A22284).

291 To visualize focal adhesion formation in 2D environments in the absence of transduction
292 with the GFP-paxillin biosensor, HFF cells were plated in ibidi μ -Slide VI^{0.4} channel slides with
293 ibiTreat surfaces (ibidi, Catalog #80606). After attaching in the presence of serum, cells were fixed
294 for 15 min at room temperature using 4% paraformaldehyde diluted in PBS. Channels were washed

295 three times with PBS, and non-specific binding was blocked for 1 h at room temperature using a
296 solution of 0.3% Triton X-100 and 20% goat serum in PBS. After blocking, channels were washed
297 three times with PBS. An anti-paxillin antibody (purified mouse anti-paxillin, clone 349, BD
298 Biosciences, San Jose, CA, Catalog #610052) was diluted 1:75 in PBS containing 1% BSA, added
299 to the cells, and incubated at 4°C overnight. Following incubation, cells were washed three times
300 in PBS. A secondary antibody solution containing a 1:200 dilution of goat anti-mouse
301 AlexaFluor™ 594 (ThermoFisher, Catalog# A11020), a 1:40 dilution of AlexaFluor™ 488
302 phalloidin (ThermoFisher, Catalog #A12379), and 1 µg/ml Hoechst 33342 (ThermoFisher,
303 Catalog #H3570) diluted in 1% BSA in PBS was added and incubated at room temperature for 1
304 h. Cells were washed five times with PBS prior to imaging.

305 **Confocal microscopy**

306 For cells embedded in 3D matrices, images were acquired on a Zeiss 780 LSM confocal
307 microscope. One-photon, confocal, 12-bit, 2-dimensional images were acquired at lateral
308 dimensions of 512x512 pixels with a Zeiss 20x Plan-Apochromat, 0.8 NA objective. Individual
309 images were tiled (3x3 grid) to image a total area of 1275.29 µm x 1275.29 µm (1536 pixels x
310 1536 pixels). Tiled images were acquired in z-stacks spaced 2 µm apart over an axial distance of
311 ~120 µm to image cells throughout the matrix. Samples were excited with 561 nm light from a
312 solid-state laser with a total power of 20 mW, 405 nm light from a laser diode with a total power
313 of 30 mW, and 488 nm light from an argon laser with a total power of 25 mW. Lasers were set at
314 or below 2.4% of the total power. Two beam splitters, MBS 488/561 and MBS 405, were employed
315 in the emission pathway to delineate the red, green, and blue channels. Transmitted light was also
316 collected. Pinhole width was set at 90 µm. Pixel dwell was set at 1.58 µs. The master gain was set
317 at or below 890 for all images acquired. For some images in Figures 1-3, confocal z stacks were

318 acquired at 2048 pixels x 2048 pixels to obtain greater detail of cell and fiber morphology. To
319 image expression of paxillin in 3D matrices, one-photon, confocal, 12-bit, 2-dimensional images
320 were acquired at lateral dimensions of 512x512 pixels with a Zeiss 40x Plan-Apochromat, 1.4 NA
321 oil immersion objective on a Zeiss 780 LSM confocal microscope. Images were acquired at 4 times
322 digital zoom to achieve a final pixel size of 0.1038 μm x 0.1038 μm . Images were acquired in z-
323 stacks spaced 1 μm apart over the height of a cell. Samples were excited with 633 nm light from a
324 solid-state laser with a total power of 5 mW, 405 nm light from a laser diode with a total power of
325 30 mW, and 488 nm light from an argon laser with a total power of 25 mW. Lasers were set at or
326 below 4% of the total power. Tracks were imaged in sequence to minimize crosstalk. Pinhole width
327 was set at 41.3 μm . Pixel dwell was set at 1.58 μs . The master gain was set at or below 700 for all
328 images acquired. Axial stacks were trimmed to contain only the images with the fibrils in focus,
329 and maximum intensity projections were made to visualize the actin cytoskeleton, nucleus, and
330 paxillin expression.

331 **Protrusion analysis for cells embedded in 3D matrices**

332 To analyze protrusion length and directionality, confocal tile scans acquired at 20x
333 magnification and axial steps of 2 μm (1275.29 μm x 1275.29 μm , 1536 pixels x 1536 pixels) were
334 opened in Fiji. Protrusions were measured only in the plane in which the fibers were in focus to
335 quantify cell response to local fibers in aligned matrices, and only for cells clearly embedded in
336 3D for unaligned matrices. The line tool in Fiji was used to draw a line from the edge of the nucleus
337 (manually identified) to the end of the protrusion to measure the protrusion length and protrusion
338 angle. In aligned matrices, the line tool was also used to draw a line on the fiber immediately
339 adjacent to the protrusion. The angle (0° - 90°) between the protrusion and the neighboring fiber
340 was calculated and recorded as the protrusion angle. For cells in unaligned matrices, the protrusion

341 angle was calculated with respect to the vertical, and all angles were then mapped to be between
342 0° and 90°. For each cell type, matrix alignment status, drug, or antibody treatment, and
343 nanoparticle ECM protein, 10-20 protrusions were measured from each 3D matrix. Statistical
344 analysis and plot generation were done in Prism GraphPad 7. The number of matrices prepared for
345 each condition is indicated in figure legends, and a matrix was used only if at least 10 cells were
346 measured. Histograms were generated to visualize the distribution of protrusion angles in aligned
347 and unaligned matrices. Protrusion lengths were compared between aligned and unaligned
348 matrices using Sidak's multiple comparisons test for a given ECM nanoparticle coating following
349 two-way ANOVA. For mechanistic experiments, protrusion lengths were compared between
350 control and treated cells for a given cell type by Dunn's multiple comparisons post-test following
351 a Kruskal-Wallis test.

352 **Analysis of matrix topography**

353 Fibers were analyzed in Matrigel matrices containing colloidal particles conjugated to
354 fibronectin, tenascin C, or laminin and HFF cells seeded for 24 h as described above. Analysis was
355 performed on maximum intensity z projections of the fluorescent channel for the fibers in 425.10
356 $\mu\text{m} \times 425.10 \mu\text{m}$ (2048 pixels x 2048 pixels), 12-bit images acquired at 20x magnification as
357 described above. Maximum intensity projections were performed on planes containing aligned
358 fibers. Images were changed to 8-bit grayscale and analyzed using the ctFIRE V2.0 toolbox [30].
359 Minimum fiber length was set at 30 pixels, and max fiber width was set at 30 pixels. Three images
360 from the same matrix were analyzed for aligned fibronectin-conjugated colloidal particles,
361 whereas one image per matrix were analyzed for matrices containing aligned tenascin C- and
362 laminin-conjugated colloidal particles. This resulted in segmentation and analysis of 7288 fibers

363 for fibronectin-conjugated particles, 4571 fibers for tenascin C-conjugated particles, and 3895
364 fibers for laminin-conjugated particles.

365 **Fluorescence recovery after photobleaching**

366 To generate matrices containing diffusible dextran, 430 μ l of Matrigel was mixed with 12
367 μ l of fibronectin- or BSA-conjugated colloidal particles (300 nm diameter) at 10 mg/ml and 50 μ l
368 of FITC dextran (fluorescein isothiocyanate dextran, average molecular weight 10 kDa, Sigma
369 Millipore, Catalog #FD10S-250MG) at 984 μ g/ml. This generated a mixture containing FITC
370 dextran at 100 μ g/ml. Proteins conjugated to colloidal particles were not fluorescently labeled so
371 as not to interfere with the dextran fluorescence signal. To generate control Matrigel matrices
372 lacking added colloidal particles, the same proportions were used, with 12 μ l of serum free media
373 replacing the 12 μ l of particle solution.

374 Matrigel/particle/dextran mixtures were plated in wells of a 4-well chamber slide coated
375 with 100 μ l/well of Matrigel, as described above. Matrices were aligned on a magnet that was
376 chilled in ice for 15 minutes as described above, or kept on ice away from the magnet for 15
377 minutes to generate unaligned matrices. The matrix was polymerized for 30 minutes at 37 °C.
378 Matrices were then hydrated with 350 μ l/well of serum free media containing 100 μ g/ml of FITC
379 dextran.

380 Fluorescence recovery after photobleaching (FRAP) experiments were carried out using
381 the FRAP module on a Zeiss 780 confocal equipped with a Zeiss 20x Plan-Apochromat, 0.8 NA
382 objective. One-photon, confocal, 12-bit, 2-dimensional images were acquired at lateral dimensions
383 of 512x512 pixels to obtain a pixel size of 0.830 μ m x 0.830 μ m. A 50 pixel x 50 pixel square
384 region of the matrices in the plane of the aligned fibers was bleached for ~30s and imaged every

385 500 msec for 240 cycles. Four scans of the region were acquired before bleaching. A reference
386 region offset from the bleached region of the same dimensions was used to account for loss of
387 signal due to repeated scanning.

388 FRAP parameters were calculated using the FRAP analysis module in Zeiss ZEN. Briefly,
389 image intensity values over time were fit to the formula:

$$390 \quad I(t) = I_E - I_1 * \exp\left(-\frac{t}{T_1}\right)$$

391 Curves were normalized to obtain mobile fractions and characteristic half maximum times using
392 the built-in calculations in ZEN:

$$393 \quad I_{normalized}(t) = A(1 - \exp(-\tau * t))$$

394 Where A = mobile fraction and the half maximum time is defined as:

$$395 \quad \tau_{1/2} = \frac{\ln 0.5}{-\tau}$$

396 For each condition (particle protein coating and alignment status), three independent regions from
397 two gels were measured. These measurements were grouped to obtain N=6 values prior to
398 statistical comparisons. Analysis was performed in GraphPad Prism 7 using two-way ANOVA
399 comparing aligned and unaligned matrices containing either fibronectin- or BSA-conjugated
400 colloidal particles, followed by Sidak's multiple comparisons test between conditions for a given
401 ECM protein.

402 **Bulk rheology**

403 Small angle oscillatory shear bulk rheology measurements were carried out at the
404 Georgetown University Institute for Soft Matter Synthesis and Metrology using an Anton Paar

405 Physica MCR 301 rheometer equipped with a PP-25 measuring plate (parallel, 25 mm diameter).
406 Gels were polymerized on 50 mm glass bottom dishes (Wilco, Amsterdam, The Netherlands,
407 Catalog #GWSB-5040). Samples were prepared with 120 μ l Matrigel on bottom of Wilco dish
408 polymerized prior to the Matrigel/bead matrix. To this, a mixture of 430 μ l Matrigel, 30 μ l SFM,
409 12 μ l paramagnetic beads, and 20 μ l of 1×10^5 /ml polystyrene beads (2×10^6 beads total). Beads
410 were 1 μ m rhodamine carboxylated fluorospheres (ThermoFisher, Catalog #F8821).

411 Samples were either aligned or unaligned as described above and were hydrated with a
412 superlayer of media for storage and transport. Media was removed with a pipette before
413 measurements. The instrument achieved contact with the sample with a trigger force of 0.1 N
414 normal and the excess gel was trimmed around the plate to ensure proper contact boundary
415 conditions. The complex modulus was measured at 1% strain at frequencies 0.1-10 Hz.
416 Measurements were carried out in duplicate.

417 **Optical tweezer-based microrheology**

418 Samples were prepared in Wilco dishes identically to those made for bulk rheology
419 measurements prior to characterization via optical tweezer-based microrheology. For complete
420 experimental details, see [31-33]. Our home-built setup consists of a 1064 nm trapping beam
421 steered by an acousto-optic deflector to oscillate the trap and a stationary 975 nm detection beam
422 that is coupled into and colocated with the trap with a dichroic before being sent into the backport
423 of an inverted microscope with a long working distance water objective and a high NA condenser.
424 Telescope lenses conjugate the optical plane at the acousto-optic deflector (AOD) to the back
425 aperture of the condenser, which is placed in Kohler illumination after the object is focused in the
426 specimen plane. Above the condenser, the detection beam is relayed to a quadrant photodiode for
427 back focal plane interferometric position detection. Each bead is positioned precisely in the center

428 of the trap by scanning it through the detection beam in three dimensions using a piezo
429 nanopositioning stage while recording the voltages from the QPD. The V-nm relation of the QPD
430 is calibrated in situ by fitting the central linear region of the detector response to scanning the bead
431 through the detection beam in the direction of the oscillations, giving β in V/nm (stuck bead
432 method). A second QPD records the position of the trapping laser to find the relative phase lag
433 between the bead and trap oscillations. The optical trap stiffness k is determined in situ from the
434 thermal power spectrum of each measured bead while the trap is stationary, using the active-
435 passive calibration method[34]. Together with β , k , and the bead's mass m and radius a , the
436 trajectories yield the complex modulus as a function of frequency, $G^*(\omega)$, of each bead's
437 surrounding microenvironment. In this equation, the complex modulus, $G^*(\omega)$, can be broken
438 down into components, with $G^*(\omega) = G'(\omega) + iG''(\omega)$, where the real part, $G'(\omega)$, is the elastic
439 component and the imaginary part, $G''(\omega)$, is the viscous component. The complex modulus, $G^*(\omega)$,
440 is calculated as $G^*(\omega) = \frac{i\omega\tilde{\gamma}_D(\omega)}{6\pi a}$, where the friction relaxation spectrum $\tilde{\gamma}_D(\omega)$ is related by the
441 equation $\tilde{\gamma}_D(\omega) + i\omega m = -\frac{k}{i\omega} \left(\frac{1}{i\omega\tilde{R}_L(\omega)} + 1 \right)$ to the active power spectrum $\tilde{R}_L(\omega) \equiv \frac{\tilde{x}_{dr}(\omega)}{-i\omega\tilde{x}_L(\omega)}$, with $\tilde{x}_L(\omega)$
442 and $\tilde{x}_{dr}(\omega)$ the Fourier transforms of the time series of the positions of the trapping laser and the
443 driven bead respectively, recorded while the trap is oscillating. The stiffness $k = \frac{\text{Re}\{\tilde{R}_L(\omega)\}}{P_V(\omega)}$ is
444 determined from the real part of the active power spectrum and the passive power spectrum,
445 $P_V(\omega) \equiv \langle |\tilde{x}_V(\omega)|^2 \rangle$, where $\tilde{x}_V(\omega)$ is the Fourier transform of the time series of the undriven bead's
446 thermally fluctuating position while the trap is held stationary. Each bead is subjected to fourteen
447 consecutive 2 s pulses, with the trap alternately oscillating or stationary. Amplitude of oscillations
448 was set to 20 nm with power of 100 mW at the back aperture. Only probes at distances exceeding

449 ~30 μm away from the cover slip surface to minimize drag in consideration of Faxen's law were
450 measured [35].

451 Samples were measured in triplicate with at least 30 beads per sample measured. Laser
452 power was set to 100 mW at the back aperture. Data were analyzed using custom MATLAB
453 programs. Experiments were controlled using custom LabVIEW programs. In Figure 1C, for each
454 distance from the nearest fiber and each measured frequency, the mean complex modulus was
455 divided by the mean complex modulus in unaligned gels, and moduli are expressed as percentages
456 of the unaligned gel complex modulus. These percentages were averaged across all frequencies to
457 obtain the plotted means and standard deviations.

458 **Cell seeding on 2D silicone substrates of known elastic modulus**

459 Cytosoft 6-well plates (Advanced BioMatrix, San Diego, CA, Catalog #5190-7EA; 0.5
460 kPa, 2 kPa, and 64 kPa elastic modulus) or standard 6-well tissue culture plastic dishes were
461 incubated with human plasma fibronectin (Millipore Sigma, Catalog #FC010) at a concentration
462 of 10 $\mu\text{g}/\text{ml}$ diluted in PBS (3 ml/well of ECM protein solution added) for 1 h at room temperature.
463 The coating solution was aspirated, and wells were washed twice with PBS. HFF or U87 cells
464 were washed with phosphate buffered saline (PBS), detached from the cell culture flask using 10
465 mM EDTA in PBS, washed once in growth medium, centrifuged at 1000 rpm for 5 min, and
466 resuspended to a concentration 100,000 cells/ml in serum free medium. To each well, 1 ml of the
467 cell suspension (100,000 cells total) and 1 ml of serum free media were added. Plates were
468 incubated overnight at 37°C prior to fixation and staining.

469 For samples plated on substrates of varying stiffness, culture media was aspirated, and 3
470 ml of 4% paraformaldehyde diluted in PBS was added to each well. Samples were fixed at room

471 temperature for 15 min and washed twice with PBS. Cells were then permeabilized with 0.1%
472 Triton X-100 in PBS for 5 min and washed twice more with PBS. A phalloidin stock solution was
473 prepared by dissolving 10 nmol of phalloidin-Atto 488 (Millipore Sigma, Catalog #49409-
474 10NMOL) in 500 μ l methanol. To fluorescently label F-actin and the nucleus, a solution containing
475 1 μ g/ml Hoechst 33258 and 20 μ l phalloidin stock/ml in 1% BSA in PBS was prepared. Cells were
476 stained with 500 μ l staining solution/well for 1 h at room temperature. Finally, wells were washed
477 twice with PBS and stored in PBS prior to imaging. For each condition, two wells per cell type
478 were prepared simultaneously.

479 For cells plated on 2D silicone substrates, imaging was carried out at 20x magnification
480 using a ThermoFisher EVOS FL Cell Imaging System. Four random fields of view were selected
481 for each well. Two wells were prepared and imaged simultaneously for each cell type and substrate
482 stiffness. A minimum of 73 cells were imaged and analyzed for each condition.

483 **Analysis of cell morphology on 2D substrates**

484 Cell morphology on 2D substrates of varying elastic modulus was analyzed using Fiji.
485 Images obtained from the F-actin channel were binarized using the default Fiji settings and
486 processed using the “Close-” function in Fiji. Dead and truncated cells were removed from the
487 images, and shapes were manually separated or joined when necessary to more closely match the
488 original images. Another investigator compared the final drawings to the original images for
489 independent verification of the results. Circularity and area were calculated from the binarized
490 images using the “Analyze Particle” function in Fiji. Measurements were made on cells in four
491 random fields of view for each well, with two wells per substrate elastic modulus prepared and
492 imaged simultaneously for each cell type. Statistics were carried out and plots were generated in
493 GraphPad Prism 7. The effects of cell type and matrix stiffness on cell area and aspect ratio were

494 analyzed using two-way ANOVA with Tukey's multiple comparisons post-tests between all
495 combination of substrate stiffnesses for a given cell type.

496 **Zebrafish experiments**

497 Animal studies were conducted under protocols approved by the National Cancer Institute
498 and the National Institutes of Health Animal Care and Use Committee. Transgenic Tg(fli:EGFP)
499 zebrafish [36] were maintained on a 14-hour light/10-hour dark cycle according to standard
500 procedures at 28.5°C. Larvae were obtained from natural spawning, raised at 28.5°C, and
501 maintained in fish water (60 mg Instant Ocean[®] sea salt [Instant Ocean, Blacksburg, VA] per liter
502 of DI water). Larvae were checked regularly for normal development. For all experiments, larvae
503 were transferred to fish water supplemented with N-phenylthiourea (PTU; Millipore Sigma,
504 Catalog #P7629-25G) between 18-22 hours post-fertilization to inhibit melanin formation. PTU
505 water was prepared by dissolving 16 µl of PTU stock (7.5% w/v in DMSO) per 40 ml of fish water.
506 Water was replaced daily.

507 For cell injections, HFF and U87 cells were detached from cell culture plates using 10 mM
508 EDTA, stained with CellTracker Deep Red membrane dye (ThermoFisher, Catalog #C34565)
509 diluted to 1 µM in PBS for 30 min at 37°C, washed with PBS, and resuspended to a concentration
510 of 1 million cells/20 µl PBS. An anesthetic of buffered tricaine was prepared by adding 4.2 ml
511 tricaine stock (400 mg tricaine powder [Millipore Sigma, Catalog #E10521-50G], 97.9 ml
512 deionized water, 2.1 ml of 1 M Tris) per 100 ml of fish water supplemented with PTU. 2 days post-
513 fertilization (dpf) Tg(fli:EGFP) larvae were anesthetized and oriented on an agarose bed. A volume
514 of 2-5 nl of the cell suspension (~100-250 cells) were injected to the zebrafish hindbrain. Zebrafish
515 were maintained for 24 h following injection at 33°C in fish water supplemented with PTU or
516 water containing 100 µM blebbistatin or vehicle control (DMSO).

517 For imaging, zebrafish were anesthetized and mounted in a lateral orientation in 1%
518 agarose in a Lak-Tek 4-well chambered coverglass well. Tricaine water was added to the well prior
519 to imaging. Images were obtained on a Zeiss 780 LSM confocal microscope. One-photon,
520 confocal, 12-bit, 2-dimensional images were acquired at lateral dimensions of 512x512 pixels with
521 a Zeiss 20x Plan-Apochromat, 0.8 NA objective, and images at axial distances of 1 μm were
522 stacked to obtain three-dimensional datasets. Images presented in Figure 6 are average intensity
523 projections.

524

525 **RESULTS**

526 **Characterization of the bulk topographical and rheological properties of engineered 3D** 527 **aligned matrices**

528 We used our recently developed platform in which we incorporate a number of human
529 proteins into the three-dimensional fibrillar architecture system [17, 37]. ECM proteins were
530 labeled with a fluorescent marker and conjugated to 300 nm-diameter carboxylated
531 superparamagnetic particles. To generate 3D matrices with embedded cells and fibers, cells were
532 mixed with Matrigel and colloidal particles and plated in coverslip-bottom chamber slides that had
533 been previously covered with a thin layer of gelled Matrigel. The slide was then either placed on
534 a magnet to generate aligned fibrils or kept far from the magnet to maintain a random dispersion
535 of particles. Finally, the slide was kept at 37°C to gel and set the nanoparticle topography, and
536 cells were incubated in the presence of serum free medium for 24 h (**Figure 1A, Supplementary**
537 **Figure 1A-C**). Aligned and unaligned matrices contained the same absolute amount of ECM

538 proteins conjugated to colloidal particles and the same number of colloidal particles per unit
539 volume within the hydrogel, differing only in the alignment status of the colloidal particles.

540 Cellular migration and cell morphology are sensitive to the compliance and viscoelasticity
541 of their immediate milieu [2, 19]. We thus characterized the mechanical properties of both aligned
542 and unaligned laminin-rich ECM (Matrigel) matrices in the absence of cells. Macroscale
543 mechanics are often determined from models where the material can be assumed to act as a
544 continuum. In order for the continuum assumption to apply, the characteristic length scale of
545 underlying structural components must be much smaller than that of the physical measurement
546 [38]. One concern relevant to characterization of the composite matrices is that the magnetic
547 particles forming the aligned fibrils are rigid, and that this property could in turn affect cell
548 phenotype. Thus, we reasoned that at the microscale, the self-assembled fibrils may give rise to
549 local variations in mechanics that will not be resolved with bulk rheology. We performed optical
550 tweezer-based active microrheology to probe heterogeneous mechanical properties in 3D
551 microenvironments on the length scales of cellular mechanotransduction (~micron) (**Figure**
552 **1B,C**). For these experiments, we focused on composite Matrigel gels containing fibronectin-
553 conjugated colloid particles. Active microrheology measurements revealed a gradient in the
554 complex modulus (G^*) as a function of distance from the assembled fiber (**Figure 1B,C;**
555 **Supplementary Figure 2A**). Regions within 1 μm of the fibers, which were comprised of rigid
556 paramagnetic particles, were stiffer than the unaligned gels, with G^* over 3-15,000 Hz ranging
557 from 0.5 – 2.5 kPa and 0.2 – 2.0 kPa for aligned and unaligned gels, respectively, with both
558 frequency ($p = 2.8\text{e-}80$) and fiber alignment ($p = 1.5\text{e-}39$) having statistically significant effects
559 on G^* by two-way ANOVA (**Figure 1B,C**). At further distances of 2–4 μm from the nearest fiber,
560 local stiffness decreased (**Figure 1B,C**). Complex modulus values at distances of 2–4 μm from the

561 nearest fiber were slightly less those than in unaligned gels (**Figure 1B,C**). The complex modulus
562 at a frequency of 3 Hz was 65 Pa, 100 Pa, and 175 Pa for beads at distances 2 μm , 3 μm , and 4
563 μm , respectively, while the complex modulus at 15,000 Hz was 300 Pa, 400 Pa, and 600 Pa for
564 these distances. The effect of distance from the fiber on complex modulus across frequencies is
565 summarized in **Figure 1C**.

566 We determined that there is a difference in frequency dependence of the complex moduli
567 in aligned vs. unaligned gels (**Figure 1B; Supplementary Figure 2**). To quantitatively assess the
568 frequency dependence of the complex moduli in these gels, we fit the complex modulus using a
569 power law model, $G^*(\omega)=A\omega^b$, where ω is the frequency. For beads 1–4 μm away from an aligned
570 fiber, the frequency dependence was similar, with G^* weakly dependent on frequency, having
571 power law fits of – 1 μm : $A=194$ (95% C.I.: 147, 241) , $b=0.24$ (95% C.I.: 0.21, 0.27), $r^2: 0.95$; 2
572 μm : $A=35$ (95% C.I.: 24, 36), $b=0.24$ (95% C.I.: 0.20, 0.28), $r^2: 0.92$; 3 μm : $A=42$ (95% C.I.: 26,
573 59), $b=0.25$ (95% C.I.: 0.21, 0.30), $r^2: 0.90$; 4 μm : $A=30$ (95% C.I.: 21, 38), $b=0.22$ (95% C.I.:
574 0.18, 0.25), $r^2=0.91$). In unaligned gels, the power law exponents were closer to the value (0.75)
575 predicted for semi-flexible polymers ($A=5$ (95% C.I.: 2, 8), $b=0.61$ (95% C.I.: 0.54, 0.68), $r^2: 0.98$).
576 In addition, the frequency dependence of the elastic and viscous contributions to the complex
577 moduli ($G^* = G' + iG''$, where G' = elastic component and G'' = viscous component) differed
578 between the aligned and unaligned gels, with crossover frequencies (at which G'' first exceeds G')
579 of ~ 1 kHz in unaligned gels and ~ 10 kHz in aligned gels (**Supplementary Figure 2**). As an
580 example, the crossover frequency in aligned matrices at a distance of 3 μm from the nearest fiber
581 was much greater than that in unaligned gels (**Supplementary Figure 2B**).

582 To assess how micron-scale rheological measurements compared to bulk rheology, we
583 characterized bulk mechanical properties of aligned and unaligned Matrigel hydrogels using

584 parallel plate small angle oscillatory shear (SAOS) bulk rheology (**Figure 1D**). Bulk rheological
585 measurements revealed that the complex moduli ($G^* = G' + iG''$, where G' = elastic component
586 and G'' = viscous component) of aligned vs unaligned (random) matrices were comparable
587 independently of the ECM coating used (**Figure 1D**). These hydrogels were mostly elastic, where
588 the shear elastic moduli ranged from 10-30 Pa with very little viscous component over the range
589 of ~0.1-100Hz (**Figure 1D**), less rigid than the ~100 Pa stiffness reported for collagen gels [39].
590 The complex moduli of Matrigel matrices containing colloidal particles were similar to the bulk
591 rheological properties of Matrigel in the absence of colloidal particles that we have reported
592 previously [17, 31]. In the low frequency regime, bulk and microrheology methods gave nearly
593 identical values for the complex modulus (**Figure 1E**). Fluorescence recovery after
594 photobleaching (FRAP) measurements of aligned and unaligned Matrigel matrices containing
595 colloidal particles conjugated to fibronectin or BSA revealed a slight decrease (~15%) in both the
596 mobile fraction and half-max time in aligned vs. unaligned gels (**Supplementary Figure 3**).
597 Values in unaligned matrices were nearly identical to those obtained in Matrigel lacking colloidal
598 particles. While alignment status was a significant sources of variation in FRAP parameters by
599 two-way ANOVA, half-maximum times in both aligned and unaligned gels were ~7-8 seconds,
600 much shorter than the overnight cell spreading times in protrusion experiments (**Supplementary**
601 **Figure 3**).

602 We next characterized the topographical properties of the engineered matrices. Matrigel
603 matrices were seeded with human foreskin fibroblasts (HFFs) and colloidal particles conjugated
604 to human fibronectin, tenascin C, or laminin, aligned, incubated for 24 h, and imaged. Individual
605 fibers were analyzed using the ctFire analysis toolbox [30] (**Figure 2A, Supplementary Figure**
606 **4**). Fibers were oriented primarily in one direction by the magnetic field (**Figure 2B**) and exhibited

607 low curvature, regardless of the ECM protein used to coat the colloidal particles (**Figure 2C**).
608 Fiber lengths were slightly longer for fibronectin- vs. tenascin C- and laminin-coated colloidal
609 particles, but for all ECM proteins, the length of an individual fiber was typically $\sim 10 \mu\text{m}$ (**Figure**
610 **2D**). Fibers were typically $\sim 1\text{-}2 \mu\text{m}$ in width, though fibers formed with tenascin C-coated
611 colloidal particles were somewhat thinner than those formed from colloidal particles formed with
612 fibronectin- or laminin-coated particles, as observed in Gaussian fits of the fiber width
613 distributions (**Figure 2E**).

614 **Human foreskin fibroblasts and glioblastoma cells respond to aligned fibrils for a myriad** 615 **of human ECM proteins in the 3D microenvironment**

616 Having characterized the physical properties of the engineered matrices, we examined
617 cellular response to aligned topographical cues using human HFF and U87 cells in Matrigel
618 matrices. Protrusions serve as sensors of the local environment. Previous work has demonstrated
619 that cells protrude along aligned topographical cues in collagen gels [40] and on microcontact-
620 printed surfaces [41], and we therefore assessed whether similar contact guidance was observed in
621 our engineered matrices. Protrusions in response to fibrillar topography were quantified in the
622 presence of colloidal particles conjugated to human fibronectin, tenascin C, and laminin prior to
623 being embedded within Matrigel. In aligned matrices, both cell types were spindle shaped and
624 formed long, actin-rich protrusions, as indicated by staining with phalloidin (displayed in red;
625 **Figure 3A**). In these aligned matrices, large (on the order of mm) areas could be patterned to
626 contain oriented fibers with exposed ECM proteins for cell binding (**Supplementary Figure 5**).
627 Cells embedded in matrices containing unaligned colloidal particles (and thus, the same absolute
628 amount of human ECM proteins) remained largely spherical and had shapes similar to that of cells
629 in Matrigel alone (**Figure 3A; Supplementary Figure 6A,B**). Additionally, the engineered

630 alignment method was amenable to the production of alignment in other matrices, including
631 agarose and hyaluronic acid (**Supplementary Figure 7**). Some particle aggregation was observed
632 in unaligned matrices, but in general, the fluorophore density of the dispersed colloidal particles
633 was not sufficient to generate a fluorescent signal. In **Figure 3A** and **Supplementary Figures 6**
634 **and 7**, insets in images of unaligned matrices show these matrices with the lookup tables adjusted
635 to demonstrate the presence of dispersed nanoparticles in the hydrogels.

636 We next asked if mature focal adhesions are formed in the aligned 3D Matrigel matrices
637 (**Figure 3B**). We transduced HFF cells with GFP-paxillin. As a control, we assessed focal adhesion
638 formation first on 2D surfaces, where immunofluorescence was performed with an antibody
639 directed against paxillin. Fluorescence images revealed large focal adhesions at the distal ends of
640 cell protrusions (**Figure 3C**). We confirmed similar distributions for cells transduced with the
641 paxillin biosensor, where images revealed both large adhesions and cytoplasmic GFP-paxillin
642 (**Figure 3D**). When transduced cells were introduced to Matrigel matrices containing aligned
643 fibrils formed of fibronectin-conjugated colloidal particles, paxillin expression was diffuse, and
644 we noted numerous instances where protrusions parallel or perpendicular the fibrils lacked plaques
645 of paxillin (**Figure 3E**), while some protrusions had small paxillin-containing adhesions (**Figure**
646 **3E**, bottom right panel). Paxillin expression was similarly diffuse in unaligned 3D matrices
647 (**Figure 3F**).

648 To quantitate the response of normal and malignant human cells in the engineered fibril
649 system, HFF and U87 cells were fixed and imaged after being embedded in aligned or unaligned
650 matrices (or Matrigel control without additional particles), and protrusion length and angle
651 compared to local fiber alignment were quantified (**Figure 4A,D**). HFF cells plated in aligned
652 matrices preferentially sent out protrusions along or perpendicular to the fibers (**Figure 4A**). In

653 contrast, cells remained spherical in unaligned matrices and extended thin, randomly oriented
654 filopodia-like protrusions (**Figure 4A**, right panel). Time-lapse videos of cells embedded in
655 aligned matrices revealed that cells typically sent out protrusions along or perpendicular to fibers
656 before locally contracting the matrix (**Supplementary Videos 1,2**). The length of protrusions of
657 cells in aligned matrices 24 h after seeding significantly increased compared to cells in unaligned
658 matrices, where protrusion lengths were similar to those seen in Matrigel alone (**Figure 4B**). The
659 local angle between fibers and cell protrusions in aligned matrices was preferentially either 0° or
660 90° (**Figure 4C**, left panel), indicating protrusions sent out parallel or perpendicular to the fibers
661 (see insets in **Figure 4A**). In unaligned matrices, protrusions were randomly distributed around
662 the cell body (**Figure 4C**, right panel). These trends held across all of the ECM protein coatings
663 tested, suggesting that the presence of a topographical cue was more important in the observed cell
664 extensions than specific integrin-ECM interactions for fibers formed in a Matrigel base matrix.
665 Although both ECM coating and matrix alignment were significant sources of variation in
666 protrusion length by two-way ANOVA, matrix alignment status was the predominant factor,
667 accounting for 46% of the observed variation, and protrusions were significantly longer in aligned
668 vs. unaligned matrices for all ECM proteins tested. The assembly of ECM protein-conjugated
669 colloidal particles into fibers could increase the local effective ligand density in the vicinity of the
670 cell compared to unaligned gels. Thus, we also conjugated bovine serum albumin (BSA), a protein
671 lacking binding moieties for cell adhesion proteins, to the colloidal particles and formed aligned
672 and unaligned gels (**Supplementary Figure 6C**). Cell response (increased protrusion length and
673 protrusion alignment to local fibers) was identical in this case (**Figure 4B,C**). We also observed
674 that paxillin expression was diffuse for cells cultured in matrices containing BSA-conjugated

675 particles, similar to what was observed in aligned matrices containing fibronectin-conjugated
676 particles (**Supplementary Figure 6D**).

677 We next asked if U87 cells showed similar behavior to the normal cell line. Similar
678 responses to matrix alignment for the diversity of ECM chemistries tested where U87 cells
679 generated protrusions preferentially parallel or perpendicular to local fibers and remaining largely
680 spherical in unaligned matrices (**Figure 4D**). U87 cells extended longer protrusions in aligned than
681 unaligned matrices for a given ECM protein (**Figure 4E**). Similar to the case seen in HFF cells,
682 both ECM protein and alignment status were significant sources of variation in protrusion length
683 by two-way ANOVA, but alignment status again accounted for the largest percentage of the
684 variation observed. Additionally, topographical cues in aligned matrices led to U87 cell
685 protrusions predominantly parallel or perpendicular to local fibers (**Figure 4F**, left panel). These
686 trends were not observed in unaligned matrices, where protrusions were again distributed around
687 the cell body instead of in preferred directions (**Figure 4F**, right panel).

688 Having determined that there were local heterogeneities in microscale mechanics in aligned
689 Matrigel matrices and that cells generated directional protrusions in response to alignment, we
690 aimed to assess how environmental stiffness regulated cell elongation. We thus characterized cell
691 phenotypic response to substrates of differing mechanical properties. Previous work has shown
692 that sensitivity to ECM substrate stiffness is dependent on the concentration of ECM ligand [16,
693 42], and we therefore compared cell morphology on substrates coated with a comparable
694 concentration of ECM protein as that conjugated to the colloidal particles (approximately 0.3
695 $\mu\text{g}/\text{cm}^2$) with stiffnesses that spanned several orders of magnitude from 0.5 kPa - >GPa
696 (**Supplementary Figure 8A**). This dynamic range allowed us to probe responses across the
697 stiffnesses of several tissues, from the brain to the bone. We determined that the cell morphology

698 and the presence of actin cytoskeletal structures in HFF and U87 cells were largely insensitive to
699 the stiffness of the underlying ECM substrate until stiffnesses reached the GPa range, well higher
700 than the difference in stiffness observed near and far from aligned fibers in the engineered system.
701 Substrate stiffness was not a significant source of variation in cell aspect ratio by two-way
702 ANOVA (**Supplementary Figure 8B**), and significant differences in areas for U87 cells were only
703 observed between the much stiffer tissue culture plastic compared to the softer silicone substrates
704 (**Supplementary Figure 8C**). HFF cell spreading was also reduced at the softest substrate stiffness
705 (0.5 kPa) compared to intermediate stiffness values (**Supplementary Figure 8C**).

706 **Integrin $\beta 1$ and fascin contribute to cell protrusion generation in aligned matrices**

707 Having observed cell protrusions similar to elongated filopodia in response to
708 topographical cues in the presence of a local gradient in micromechanics, we set out to understand
709 mechanistic drivers of cell response within 3D substrates by interrogating processes implicated in
710 protrusion generation (**Figure 5A,B**). We focused on Matrigel matrices containing aligned fibers
711 formed of fibronectin-conjugated colloidal particles. Cells use integrin-rich filopodia adhesions to
712 sense ECM gradients. We thus reasoned that integrin $\beta 1$ may be a key regulator needed for the
713 observed elongation and alignment of cellular protrusions. Silencing integrin $\beta 1$ using siRNA
714 significantly reduced the average length of protrusions formed for both HFF and U87 cells in
715 aligned 3D matrices (**Figure 5B-C, Supplementary Figure 9A**). However, the protrusion angle
716 relative to the angle of the nearest fiber was not changed upon knockdown (**Figure 5D,E**). Similar
717 results were obtained upon treatment with a function-blocking antibody directed against integrin
718 $\beta 1$ (**Supplementary Figure 9B-D**). Extension of a filopodium is driven by a fascin-dependent
719 bundling of actin filaments. Inhibition of fascin, using the inhibitor fascin-G2 (**Figure 5A,B**), had
720 a similar effect as knockdown of integrin $\beta 1$, shortening protrusion lengths while not affecting

721 protrusion angles (**Figure 5F-H**). In summary, inhibition of integrin $\beta 1$ and fascin tended to result
722 in cells remaining fairly rounded in aligned matrices (**Figure 5B**).

723 **Myosin II contributes to cell alignment in response to local topographical and stiffness**
724 **gradients both in vitro and in vivo**

725 As myosin II has been implicated in cell mechanosensing [25], we treated cells with the
726 myosin II inhibitor, blebbistatin, and quantified cellular protrusions in aligned Matrigel matrices
727 containing fibronectin-conjugated particles (**Figure 6A-E**). Upon treatment with blebbistatin, cells
728 embedded in the matrices formed numerous long, spindly protrusions that were not well-aligned
729 to the fibers (**Figure 6B**), and average protrusion length upon blebbistatin treatment remained
730 unchanged in HFF cells and increased in U87 cells (**Figure 6C**). However, blebbistatin treatment
731 inhibited alignment of protrusions to the engineered fibers, particularly in HFF cells, where the
732 distribution of angles to the fibers was flattened upon inhibition of contractility (**Figure 6D**).
733 Expression of paxillin by HFF cells in aligned matrices remained diffuse upon treatment with
734 blebbistatin (**Supplementary Figure 10**). The phenomenon of decreased protrusion alignment to
735 the fibers was observed to a somewhat lesser extent in U87 cells (**Figure 6E**).

736 Aligned structures in vivo span varying lengths, from ECM fibers to guidance cues
737 received from co-opting blood vessels. One question concerns whether the thickness of the fibers
738 as well as the alignment is important in driving cell response. In our system, the fibrils were ~ 1 - 2
739 μm in thickness but show persistence of several microns. Thus, to begin assessing in vivo
740 relevance, we employed an animal model wherein cell response to a topographical cue was readily
741 observable via intravital microscopy. We injected HFF and U87 cells to the hindbrain of 2 days
742 post fertilization (2 dpf) larval Tg(fli:EGFP) zebrafish, which are largely transparent and in which
743 vascular endothelial cells express EGFP (**Figure 6F**). At 2 dpf, vessels in the zebrafish brain are

744 wider than the fibers formed in the in vitro system (typically ~10-20 μm in width), with several
745 regions in each fish where they were linear on the scale of a cell body length (**Figure 6G**).

746 We injected cells stained with a membrane dye to the zebrafish hindbrain and incubated
747 the fish and cells for 24 hours post-injection in water supplemented with 100 μM Blebbistatin or
748 the appropriate vehicle control (**Figure 6F**). To assess cell spreading in response to topographical
749 cues, we imaged cells in the vicinity of blood vessels. Under control conditions, both HFF and
750 U87 cells proximal to topographical cues elongated and extended protrusions, usually parallel to
751 the long axis of the vessels (arrows, **Figure 6H** and **Supplementary Figure 11**). While protrusions
752 were typically parallel to the vessels, some cells elongated perpendicular to these cues (**Figure**
753 **6H**, left panel), similar to our observations in the in vitro system. In contrast, cells away from
754 vessels remained rounded (**Figure 6H**, asterisks, and **Supplementary Figure 11**). To assess
755 whether inhibiting contractility would affect alignment in vivo in a similar manner to that observed
756 in the engineered in vitro system, we treated a subset of U87 cells with 100 μM Blebbistatin
757 overnight. Blebbistatin-treated U87 cells remained rounded along blood vessels (**Figure 6I**, left
758 panel) or sent out thin, spindle-shaped protrusions in the absence of topographical cues, similar to
759 what was observed in vitro (**Figure 6I**, right panel).

760

761 **DISCUSSION**

762 The ECM provides important chemical signals within native tissue [2, 19]. In addition,
763 physical properties of the microenvironment, such as tissue mechanics and surface topography,
764 have been shown to modulate gene expression [2, 19]. In the model described here, cells receive a
765 myriad of physical cues, namely microscale heterogeneities in rigidity, topographical cues due to

766 the presence of aligned fibrils, and chemical signals from the matrix and assembled fibers. Using
767 active microrheology, we quantified the mechanical variations present within a few micrometers
768 of assembled fibers in the Matrigel matrix that was not resolved at the mm length scale using bulk
769 rheology. We then used this system to characterize how cells respond to well-defined, introduced
770 anisotropy in 3D for different types of ECM proteins. In this system, we assessed the first point of
771 contact that cells make with the ECM, that is, formation of protrusions after embedding in a 3D
772 environment. We used pharmacological and genetic perturbations of key proteins regulating
773 protrusion dynamics and cell contractility to gain insights into the mechanisms governing this cell
774 response. We determined that perturbation of myosin II abrogated the cells' ability to "sense" the
775 topographical cues.

776 Microscale mechanics are dependent upon local mesh geometry [43]. One concern is that
777 the magnetic particles are rigid and thus will introduce local heterogeneities on the micrometer
778 scale that may influence cell behavior. Compared to beads measured in unaligned gels, beads
779 within one micrometer of the nearest fiber in aligned gels were significantly more rigid, whereas
780 rigidity decreased with distance at 2-4 μm and was lower than in unaligned gels, possibly owing
781 to changes in local concentration in the background matrix due to interactions with the nanochain
782 fibers. Thus, one reason for the observed microrheological differences may be that the mesh size
783 in aligned hydrogels differs from that in unaligned hydrogels. However, in our previous work [17],
784 FRAP measurements using 150 kDa dextran indicated no differences in recovery in unaligned and
785 aligned hydrogels compared to Matrigel alone. We confirmed these findings using a lower
786 molecular weight dextran (10 kDa) in this work. The stiffness gradients observed in this work may
787 contribute to protrusion generation or stabilization. Previous work has demonstrated that
788 fibroblasts generate and retract protrusions to sense the underlying substrate stiffness [25], and that

789 cell-scale increases in matrix stiffness near bundled collagen fibrils contribute to increased stability
790 of cell adhesions to promote adhesion maturation in response to matrix alignment [44]. The
791 increased matrix elasticity near the engineered fibrils presented here may direct or stabilize
792 protrusions parallel to the fibers in a similar fashion. Protrusions directed perpendicular to the
793 fibers are potentially initially directed along the nanogrooves between paramagnetic particles.
794 Following protrusion generation, cell contractility may further deform the matrix to locally align
795 protrusions and assembled fibrils.

796 In addition to differences in the magnitude of the complex modulus, we observed a
797 difference in frequency dependence between the aligned gels and unaligned gels. Power law
798 dependence of the complex modulus on frequency has been previously observed in a number of
799 biomaterials, and various models have been proposed to explain this behavior according to the
800 underlying dynamics of the constituent polymers (47-50). In fibrillar collagen gels polymerized at
801 2 mg/ml or 6 mg/ml at 4°C or 37°C, we previously observed power law exponents ranging from
802 0.66 – 0.74 [33], in the range predicted for a semi-flexible polymer network. Here, we observed
803 exponents of ~0.6 in unaligned gels but only ~0.25 near fibers in aligned gels. Crossover
804 frequencies at which G'' exceeds G' correspond to characteristic relaxation times and reflect the
805 intrinsic time scale of energy dissipation processes inside the material. In the previously measured
806 collagen gels, crossovers occurred at 300 Hz for the gels with fine mesh of small fibers and 2750
807 Hz for the gels with larger mesh and thicker, longer fibers [33]. Here, we observed unaligned gel
808 crossovers at 1kHz and aligned gel crossovers at 10 kHz. At frequencies greater than 500 Hz, few
809 physiological processes such as ion channel gating have been documented that might be influenced
810 by external cues in this dynamic range [45]. Nevertheless, it remains to be seen how such a
811 transition will modulate cell phenotypes.

812 At the level of matrix topography, we previously determined that the viscosity of the gel,
813 concentration of the colloid particle, and duration of the applied magnetic field regulated the size
814 and length of the fibers and interfiber spacing [17]. Here, using an alignment time of 15 minutes
815 and a Matrigel 3D matrix, we obtained fibers of width $\sim 1\text{-}2\ \mu\text{m}$, somewhat thinner than those
816 observed in human dermis, which contains thick, long collagen bundles ranging from $\sim 20\text{-}50\ \mu\text{m}$
817 in diameter surrounded by a mesh of finer collagen fibers [46]. Overall, matrix organization was
818 similar to that observed in human lung tumor slices, where stromal protein density and
819 organization are variable (and includes regions with nearly parallel fibers), and gap sizes between
820 fibronectin and collagen fibers range from $\sim 5\text{-}15\ \mu\text{m}$ [47], and in lymphocyte-rich areas (for
821 example, in the lymph nodes) in humans and mice, which contain thin fibronectin fibers with
822 average spacing of $\sim 15\ \mu\text{m}$ and gaps ranging from 5 to $>30\ \mu\text{m}$ [47, 48]. Thus, cells were presented
823 with three-dimensional topographies similar to those in ECM matrices *in vivo*. Aligned
824 topographies are well-known drivers of cell polarization [49, 50].

825 Differences in the ECM proteins surrounding cells can also influence phenotype. Both
826 normal and tumor cells secrete copious amounts of ECM proteins, and an overabundance of several
827 ECM proteins is associated with abnormal tissue pathology [2]. In the case of cancer, tumor-
828 conditioned stromal cells at both sites of primary tumors and metastases secrete copious amounts
829 of proteins. Specifically, astrocytes secrete tenascin C within the brain, whereas fibroblasts secrete
830 fibronectin in response to tumor derived cytokines [51-53]. Therefore, physiologically relevant
831 biomaterials models would ideally incorporate both human cells and human matrix proteins, which
832 we include by conjugating different ECM proteins to the magnetic particles forming the aligned
833 fibers. For both HFF and U87 cells embedded in Matrigel matrices with aligned fibers, protrusion
834 lengths increased and protrusion angles became oriented relative to the fibers in comparison to

835 unaligned matrices, independent of the chemistry of the particles. Increased protrusion lengths in
836 aligned matrices with BSA-conjugated particles compared to those in unaligned matrices and
837 hydrogels devoid of particles suggest that protrusions in aligned matrices were not simply the
838 result of higher local ECM protein density from the assembled fibers. Additionally, these results
839 suggest that tumor cells may also use a similar mechanism to respond to topography as normal
840 mesenchymal cells. However, we cannot rule out that cells behaved similarly simply because they
841 may be using the same receptor to bind to these proteins. Moreover, cellular production of adhesion
842 proteins could also contribute to generation of cell protrusions. We also note that the characteristics
843 of the underlying matrix, for example, the ability of cells to break down non-porous matrices,
844 effects cell behavior. The flexibility of the matrix engineering process opens the door for
845 incorporating aligned fibers within chemically tunable 3D matrices to incorporate both
846 topographical cues from alignment and mechanical and chemical properties characteristic of a
847 given organ microenvironment.

848 Mechanistically, integrins act as the transmembrane anchor between the cell and the ECM,
849 and other studies have elegantly elucidated role of adhesion-scale ECM presentation and integrin
850 binding [54]. Heterodimers of an alpha and beta integrin subunits are used by cells for specificity
851 of ECM binding. FN, tenascin C, and laminin are known to be ligands for $\beta 1$ integrin with alpha
852 subunits of alpha5, alpha6, and alpha9, respectively [22, 51, 53]. A migrating cell responds to local
853 mechano-chemical cues by polarizing the membrane, with protrusions such as filopodia and
854 lamellipodia at the leading edge [55]. Integrin β subunits are transported in the leading edge and
855 facilitate binding with the ECM, which then drives a cascade of signals that may result in motility
856 or proliferation. Integrin $\beta 1$ has also been implicated as a key protein used by cells in contact
857 guidance [26] and in protrusion generation to aligned collagen fibers [40]. Similarly, cells cultured

858 on 2D grooves comparable in size to individual focal adhesions polarize along nanogrooves in a
859 β 1-integrin dependent manner, whereas fibroblasts cultured on nanocolumns show an increase in
860 the number of filopodia [56, 57]. Thus, we interrogated the role of β 1 integrin in regulating the
861 observed cellular behavior and found that knocking down integrin β 1 reduced the of generated
862 protrusions in aligned Matrigel matrices. However, these protrusions coaligned with the
863 engineered fibrils. While the presence of β 1 integrin was necessary for protrusion generation, we
864 did not observe large, mature focal adhesions in protrusions oriented parallel or perpendicular to
865 the engineered fibrils in our system. This diffuse paxillin staining in response to uniaxial alignment
866 cues is reminiscent of that recently observed in MDA-MB-468 cells on microcontact printed
867 collagen lines [58]. Additionally, the size of paxillin-containing focal adhesions decreases for
868 fibroblasts plated on viscoelastic vs. elastic 2D substrates, possibly due to energy dissipation due
869 to the viscosity of the microenvironment and independent of the ECM protein presented on the
870 surface [59]. This finding suggests that the viscoelasticity of the 3D matrix used in our studies may
871 contribute to a loss of large focal adhesion plaques, even in the presence of alignment cues.

872 Because fascin is the main actin-bundling protein in filopodia, we reasoned that it may also
873 be involved in protrusion generation in response to the aligned fibers within the Matrigel
874 hydrogels. Using an inhibitor that specifically blocks fascin-dependent filopodial formation, we
875 observed that the length of protrusions was reduced, while the ability to be aligned to the fibrillar
876 structures remained intact. Fascin inhibition in *in vitro* and *in vivo* migration and metastasis assays
877 show a reduction of cell migration and metastasis, and overexpression of fascin in 3D aggregates
878 of mouse mammary epithelial cells cultured 3D collagen gels show a modest ability to sense
879 aligned collagen fibers [60, 61]. Reductions in metastasis upon inhibition of fascin *in vivo* may

880 therefore be partially due to decreased sensitivity to topographical cues, which have been
881 implicated in metastatic progression [62].

882 Myosin II can affect the net rate of cellular protrusions such as lamellipodia and lamellae
883 [63]. Inhibition with blebbistatin eradicates large actin bundles in the lamellum but the
884 lamellipodium remains intact for cells cultured in 2D [63]. It further inhibits coalescence of actin
885 into proto-bundles at the lamellipodium–lamellum interface which in turn increases protrusions
886 [63]. Previous studies on 2D patterned substrates revealed that area and orientation of lamellipodial
887 protrusions contribute to contact guidance [64]. In our 3D system comprised of fibronectin-
888 conjugated particles aligned in a Matrigel hydrogel, the length of the protrusions following
889 blebbistatin treatment remained unchanged for human fibroblasts and increased in U87
890 glioblastoma cells for the given concentration. Moreover, Myosin II mediates local cortical tension
891 to guide endothelial cell branching morphogenesis and migration in 3D [65]. In the case of the
892 human fibroblasts, the protrusions were randomly oriented. On the other hand, for the case of the
893 GBM cells, even though the distribution of aligned protrusions is less robust than in the control
894 case, there is still a fraction of protrusions that are aligned to the external fibers in our 3D cultures.
895 GBM cells have been shown to be extremely plastic, and a given population is highly
896 heterogeneous [66]. Thus, there may be cells within the population that are not as dependent on
897 myosin II-mediated contractility. Taken together, these results suggest that understanding tissue
898 heterogeneities may be important in modulating the response to both topographical and
899 micromechanical cues.

900 Finally, cellular guidance and topographical cues in vivo are diverse and include fibrillar
901 structures, such as collagen networks in tendons and the dermal layer in the skin, dense ECM
902 networks, such as the basement membrane providing support to epithelial organs, and blood

903 vessels [50, 67]. Vascular co-option is one strategy used by tumor cells to access nutrients in order
904 to proliferate at distant sites [68, 69], and in cases of metastasis to the brain and breast, melanoma
905 and lung cancer cells have been found to interact with the undulating basement membrane along
906 the curvature of the existing blood vessels [68, 69]. Hence, cells respond to topographical cues for
907 both thick and thin structures, and we examined whether cellular response to aligned fibrils in vitro
908 could be extended to an in vivo system. We focused on U87 glioblastoma cells injected to the
909 zebrafish hindbrain. Glioblastomas are highly migratory, where migration on brain vasculature
910 facilitate widespread dissemination in vivo [70], and the mammalian and zebrafish brain share a
911 number of similarities [71]. Upon injection, U87 cells in proximity to topographical cues from
912 blood vessels extended protrusions parallel or perpendicular to the vessels. In contrast, blebbistatin
913 treatment was sufficient to reduce alignment with blood vessels, and U87 cells also showed
914 random protrusions away from blood vessels. Within the brain, glioma cells migrate like
915 nontransformed, neural progenitor cells, extending a prominent leading cytoplasmic process
916 followed by a burst of forward movement by the cell body that requires myosin II [66]. Thus,
917 myosin II-regulated cell contractility may also be important in topographical sensing.

918

919 **CONCLUSIONS**

920 We aimed to understand how cells respond to defined topographical cues within a 3D
921 viscoelastic hydrogel. First, we integrated human cells and ECM proteins into a 3D hydrogel
922 system containing aligned fibrils, where both cell type and ECM proteins reflect homotypic
923 interactions, and characterized the micron-scale mechanical cues that cells receive in the vicinity
924 of the fibrils. Optical-trap based active microrheology measurements revealed a local stiffness
925 gradient in the vicinity of aligned fibrils when those fibrils are formed in Matrigel. This increased

926 elasticity proximal to fibrils was similar to that observed in fibrillar collagen gels [44]. Human
927 fibroblast and glioblastoma cells seeded in aligned Matrigel matrices generated longer protrusions
928 than cells in unaligned matrices, and these protrusions were predominantly parallel or
929 perpendicular to the local fiber orientation, independently of the ECM protein coating of the
930 paramagnetic beads aligned to generate the fibrils. We observed that paxillin, a marker of stable
931 focal adhesions, was mainly diffuse, even for cells cultured in hydrogels with aligned fibers. The
932 effects of micron-scale stiffness gradients on the generation of protrusions must be considered
933 when using this system. However, we note that the aspect ratios of HFF and U87 cells were
934 unchanged when seeded on substrates ranging in stiffness from 0.5 kPa to 64 kPa, a larger dynamic
935 range than that observed in the vicinity of the fibers (**Supplementary Figure 8**). Protrusion
936 generation in aligned Matrigel matrices was dependent on both $\beta 1$ integrin expression and fascin
937 activity. However, protrusion alignment was governed in part by cell contractility. Taken together,
938 these results suggest that there is an interplay between cell contractility and sensing topographical
939 cues. The biomimetic platform presented here can be further tuned to provide fundamental insights
940 into aberrant cell mechanosensing in physiologically-relevant microenvironments.

941

942 **ACKNOWLEDGMENTS**

943 This research was supported by the Intramural Research Program of the National Institutes of
944 Health, the National Cancer Institute. We thank Daniel Blair and Xinran Zhang and the Institute
945 for Soft Matter Synthesis and Metrology at Georgetown University for access to and assistance
946 with bulk rheology measurements. We also thank Ken Yamada, NIDCR, NIH for the kind gift of
947 HFF cell lines. We thank Jayne Stommel, NCI, NIH for the kind gift of U87 cell lines. A. Hruska
948 received a NIH GSOAR Summer fellowship.

949

950 **COMPETING INTERESTS STATEMENT**

951 The authors declare no competing interests.

952

953 **DATA AVAILABILITY**

954 The raw data required to reproduce these findings are available from Kandice Tanner, Ph.D., 37
955 Convent Dr., Bethesda, MD 20852. Email: kandice.tanner@nih.gov. The processed data required
956 to reproduce these findings are available from Kandice Tanner, Ph.D., 37 Convent Dr., Bethesda,
957 MD 20852. Email: kandice.tanner@nih.gov.

958

959 **REFERENCES**

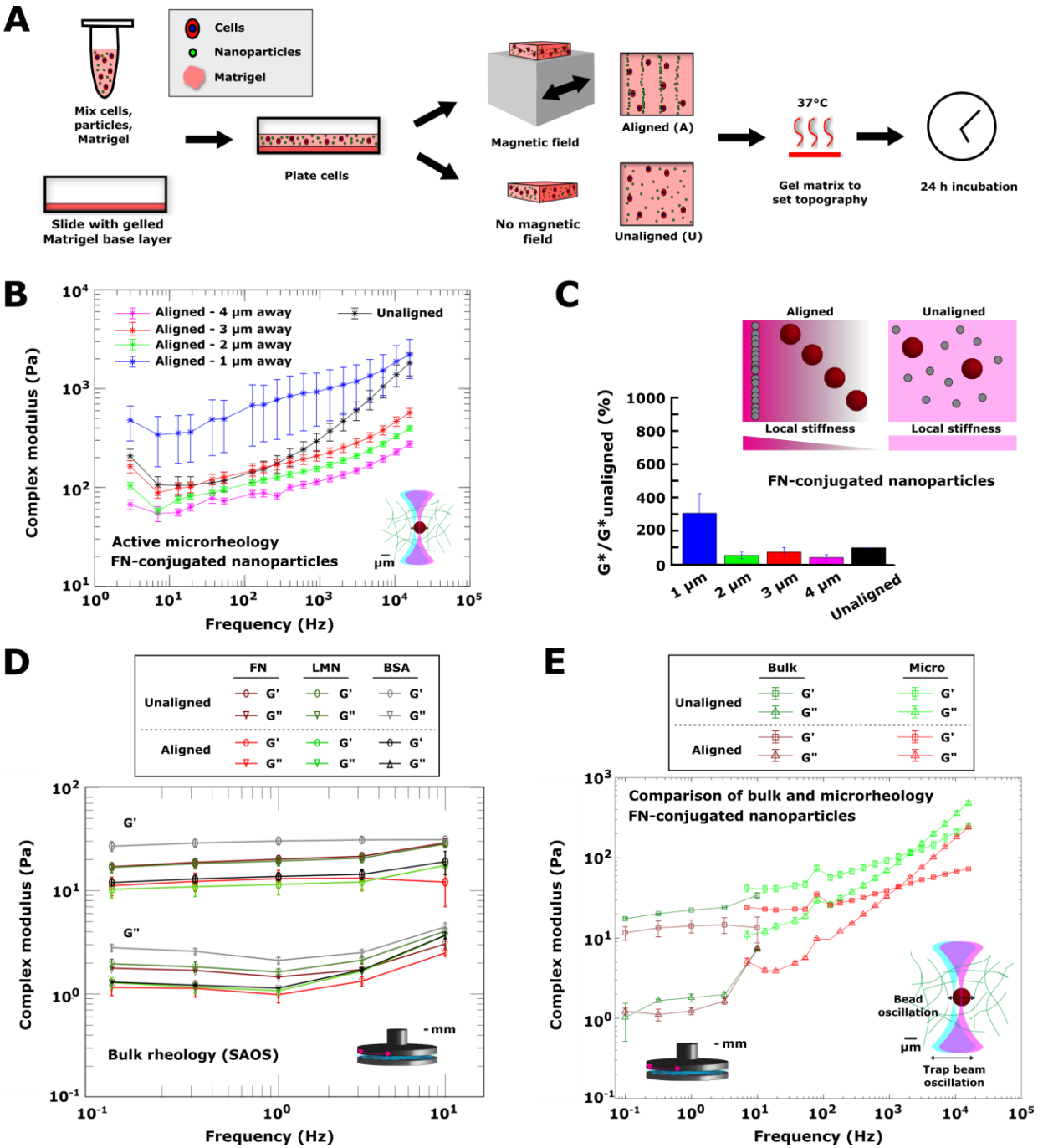
- 960 [1] Kumar S, Weaver VM. Mechanics, malignancy, and metastasis: the force journey of a tumor cell. *Cancer*
961 *Metastasis Rev.* 2009;28:113-27.
- 962 [2] Lu P, Weaver VM, Werb Z. The extracellular matrix: a dynamic niche in cancer progression. *J Cell Biol.*
963 2012;196:395-406.
- 964 [3] Tanner K, Gottesman MM. Beyond 3D culture models of cancer. *Sci Transl Med.* 2015;7:283ps9.
- 965 [4] Tenney RM, Discher DE. Stem cells, microenvironment mechanics, and growth factor activation. *Curr*
966 *Opin Cell Biol.* 2009;21:630-5.
- 967 [5] Xu R, Boudreau A, Bissell MJ. Tissue architecture and function: dynamic reciprocity via extra- and intra-
968 cellular matrices. *Cancer Metastasis Rev.* 2009;28:167-76.
- 969 [6] Bissell LL, Beebe DJ, Sung KE. Microfluidic model of ductal carcinoma in situ with 3D, organotypic
970 structure. *BMC Cancer.* 2015;15:12.
- 971 [7] Chaudhuri O, Koshy ST, Branco da Cunha C, Shin JW, Verbeke CS, Allison KH, et al. Extracellular matrix
972 stiffness and composition jointly regulate the induction of malignant phenotypes in mammary epithelium.
973 *Nat Mater.* 2014;13:970-8.
- 974 [8] Engler AJ, Sen S, Sweeney HL, Discher DE. Matrix elasticity directs stem cell lineage specification. *Cell.*
975 2006;126:677-89.
- 976 [9] Levental KR, Yu H, Kass L, Lakins JN, Egeblad M, Erler JT, et al. Matrix crosslinking forces tumor
977 progression by enhancing integrin signaling. *Cell.* 2009;139:891-906.
- 978 [10] Lin CH, Pelissier FA, Zhang H, Lakins J, Weaver VM, Park C, et al. Microenvironment rigidity modulates
979 responses to the HER2 receptor tyrosine kinase inhibitor lapatinib via YAP and TAZ transcription factors.
980 *Mol Biol Cell.* 2015;26:3946-53.

- 981 [11] Mouw JK, Yui Y, Damiano L, Bainer RO, Lakins JN, Acerbi I, et al. Tissue mechanics modulate microRNA-
982 dependent PTEN expression to regulate malignant progression. *Nat Med.* 2014;20:360-7.
- 983 [12] Paszek MJ, Zahir N, Johnson KR, Lakins JN, Rozenberg GI, Gefen A, et al. Tensional homeostasis and
984 the malignant phenotype. *Cancer Cell.* 2005;8:241-54.
- 985 [13] Provenzano PP, Cuevas C, Chang AE, Goel VK, Von Hoff DD, Hingorani SR. Enzymatic targeting of the
986 stroma ablates physical barriers to treatment of pancreatic ductal adenocarcinoma. *Cancer Cell.*
987 2012;21:418-29.
- 988 [14] Provenzano PP, Eliceiri KW, Campbell JM, Inman DR, White JG, Keely PJ. Collagen reorganization at
989 the tumor-stromal interface facilitates local invasion. *BMC Med.* 2006;4:38.
- 990 [15] Provenzano PP, Eliceiri KW, Inman DR, Keely PJ. Engineering three-dimensional collagen matrices to
991 provide contact guidance during 3D cell migration. *Curr Protoc Cell Biol.* 2010;Chapter 10:Unit 10 7.
- 992 [16] Pathak A, Kumar S. Independent regulation of tumor cell migration by matrix stiffness and
993 confinement. *Proc Natl Acad Sci U S A.* 2012;109:10334-9.
- 994 [17] Kim J, Staunton JR, Tanner K. Independent Control of Topography for 3D Patterning of the ECM
995 Microenvironment. *Advanced materials (Deerfield Beach, Fla).* 2016;28:132-7.
- 996 [18] Kim J, Tanner K. Recapitulating the Tumor Ecosystem Along the Metastatic Cascade Using 3D Culture
997 Models. *Front Oncol.* 2015;5:170.
- 998 [19] Ross AM, Jiang Z, Bastmeyer M, Lahann J. Physical aspects of cell culture substrates: topography,
999 roughness, and elasticity. *Small.* 2012;8:336-55.
- 1000 [20] Tamiello C, Buskermolen AB, Baaijens FP, Broers JL, Bouten CV. Heading in the Right Direction:
1001 Understanding Cellular Orientation Responses to Complex Biophysical Environments. *Cellular and*
1002 *molecular bioengineering.* 2016;9:12-37.
- 1003 [21] DuFort CC, Paszek MJ, Weaver VM. Balancing forces: architectural control of mechanotransduction.
1004 *Nat Rev Mol Cell Biol.* 2011;12:308-19.
- 1005 [22] Mao Y, Schwarzbauer JE. Fibronectin fibrillogenesis, a cell-mediated matrix assembly process. *Matrix*
1006 *Biol.* 2005;24:389-99.
- 1007 [23] Kubow KE, Vukmirovic R, Zhe L, Klotzsch E, Smith ML, Gourdon D, et al. Mechanical forces regulate
1008 the interactions of fibronectin and collagen I in extracellular matrix. *Nat Commun.* 2015;6:8026.
- 1009 [24] Doyle AD, Wang FW, Matsumoto K, Yamada KM. One-dimensional topography underlies three-
1010 dimensional fibrillar cell migration. *J Cell Biol.* 2009;184:481-90.
- 1011 [25] Wong S, Guo WH, Wang YL. Fibroblasts probe substrate rigidity with filopodia extensions before
1012 occupying an area. *Proc Natl Acad Sci U S A.* 2014;111:17176-81.
- 1013 [26] Paul CD, Shea DJ, Mahoney MR, Chai A, Laney V, Hung WC, et al. Interplay of the physical
1014 microenvironment, contact guidance, and intracellular signaling in cell decision making. *FASEB journal :*
1015 *official publication of the Federation of American Societies for Experimental Biology.* 2016;30:2161-70.
- 1016 [27] Lee P, Lin R, Moon J, Lee LP. Microfluidic alignment of collagen fibers for in vitro cell culture. *Biomed*
1017 *Microdevices.* 2006;8:35-41.
- 1018 [28] Tanner K. Regulation of the basement membrane by epithelia generated forces. *Phys Biol.*
1019 2012;9:065003.
- 1020 [29] Kim J, Tanner K. Three-Dimensional Patterning of the ECM Microenvironment Using Magnetic
1021 Nanoparticle Self Assembly. *Current protocols in cell biology.* 2016;25.3. 1-3. 14.
- 1022 [30] Liu Y, Keikhosravi A, Mehta GS, Drifka CR, Eliceiri KW. Methods for Quantifying Fibrillar Collagen
1023 Alignment. In: Rittié L, editor. *Fibrosis: Methods and Protocols.* New York, NY: Springer New York; 2017.
1024 p. 429-51.
- 1025 [31] Blehm BH, Devine A, Staunton JR, Tanner K. In vivo tissue has non-linear rheological behavior distinct
1026 from 3D biomimetic hydrogels, as determined by AMOTIV microscopy. *Biomaterials.* 2016;83:66-78.
- 1027 [32] Staunton JR, Blehm B, Devine A, Tanner K. In situ calibration of position detection in an optical trap
1028 for active microrheology in viscous materials. *Opt Express.* 2017;25:1746-61.

- 1029 [33] Staunton JR, Vieira W, Fung KL, Lake R, Devine A, Tanner K. Mechanical properties of the tumor
1030 stromal microenvironment probed in vitro and ex vivo by in situ-calibrated optical trap-based active
1031 microrheology. *Cellular and molecular bioengineering*. 2016;9:398-417.
- 1032 [34] Fischer M, Berg-Sørensen K. Calibration of trapping force and response function of optical tweezers
1033 in viscoelastic media. *Journal of Optics A: Pure and Applied Optics*. 2007;9:S239.
- 1034 [35] Neuman KC, Block SM. Optical trapping. *Rev Sci Instrum*. 2004;75:2787-809.
- 1035 [36] Lawson ND, Weinstein BM. In vivo imaging of embryonic vascular development using transgenic
1036 zebrafish. *Developmental biology*. 2002;248:307-18.
- 1037 [37] Kim J, Tanner K. Three-Dimensional Patterning of the ECM Microenvironment Using Magnetic
1038 Nanoparticle Self Assembly. *Curr Protoc Cell Biol*. 2016;70:25 3 1- 3 14.
- 1039 [38] Humphrey JD. Vascular Adaptation and Mechanical Homeostasis at Tissue, Cellular, and Sub-cellular
1040 Levels. *Cell Biochemistry and Biophysics*. 2008;50:53-78.
- 1041 [39] Wolf K, Te Lindert M, Krause M, Alexander S, Te Riet J, Willis AL, et al. Physical limits of cell migration:
1042 control by ECM space and nuclear deformation and tuning by proteolysis and traction force. *J Cell Biol*.
1043 2013;201:1069-84.
- 1044 [40] Carey SP, Goldblatt ZE, Martin KE, Romero B, Williams RM, Reinhart-King CA. Local extracellular
1045 matrix alignment directs cellular protrusion dynamics and migration through Rac1 and FAK. *Integr Biol*
1046 (Camb). 2016;8:821-35.
- 1047 [41] Ramirez-San Juan GR, Oakes PW, Gardel ML. Contact guidance requires spatial control of leading-
1048 edge protrusion. *Molecular biology of the cell*. 2017;28:1043-53.
- 1049 [42] Peyton SR, Putnam AJ. Extracellular matrix rigidity governs smooth muscle cell motility in a biphasic
1050 fashion. *J Cell Physiol*. 2005;204:198-209.
- 1051 [43] Wirtz D. Particle-tracking microrheology of living cells: principles and applications. *Annual review of*
1052 *biophysics*. 2009;38:301-26.
- 1053 [44] Doyle AD, Carvajal N, Jin A, Matsumoto K, Yamada KM. Local 3D matrix microenvironment regulates
1054 cell migration through spatiotemporal dynamics of contractility-dependent adhesions. *Nature*
1055 *communications*. 2015;6:8720.
- 1056 [45] Doyle DA. Structural changes during ion channel gating. *Trends Neurosci*. 2004;27:298-302.
- 1057 [46] Wolf K, Alexander S, Schacht V, Coussens LM, von Andrian UH, van Rheenen J, et al. Collagen-based
1058 cell migration models in vitro and in vivo. *Seminars in cell & developmental biology*. 2009;20:931-41.
- 1059 [47] Salmon H, Franciszkiewicz K, Damotte D, Dieu-Nosjean M-C, Validire P, Trautmann A, et al. Matrix
1060 architecture defines the preferential localization and migration of T cells into the stroma of human lung
1061 tumors. *The Journal of Clinical Investigation*. 2012;122:899-910.
- 1062 [48] Bajénoff M, Egen J, Koo LY, Laugier JP, Brau F, Glaichenhaus N, et al. Stromal Cell Networks Regulate
1063 Lymphocyte Entry, Migration, and Territoriality in Lymph Nodes. *Immunity*. 2006;25:989-1001.
- 1064 [49] Paul CD, Hung W-C, Wirtz D, Konstantopoulos K. Engineered Models of Confined Cell Migration.
1065 *Annual review of biomedical engineering*. 2016;18:159-80.
- 1066 [50] Paul CD, Mistriotis P, Konstantopoulos K. Cancer cell motility: lessons from migration in confined
1067 spaces. *Nat Rev Cancer*. 2017;17:131-40.
- 1068 [51] Hsia HC, Schwarzbauer JE. Meet the tenascins: multifunctional and mysterious. *J Biol Chem*.
1069 2005;280:26641-4.
- 1070 [52] Mueller MM, Fusenig NE. *Tumor-associated fibroblasts and their matrix*. Dordrecht ; New York:
1071 Springer; 2011.
- 1072 [53] Orend G, Chiquet-Ehrismann R. Tenascin-C induced signaling in cancer. *Cancer Lett*. 2006;244:143-
1073 63.
- 1074 [54] Geiger B, Yamada KM. Molecular architecture and function of matrix adhesions. *Cold Spring Harbor*
1075 *perspectives in biology*. 2011;3.
- 1076 [55] Baker EL, Zaman MH. The biomechanical integrin. *J Biomech*. 2010;43:38-44.

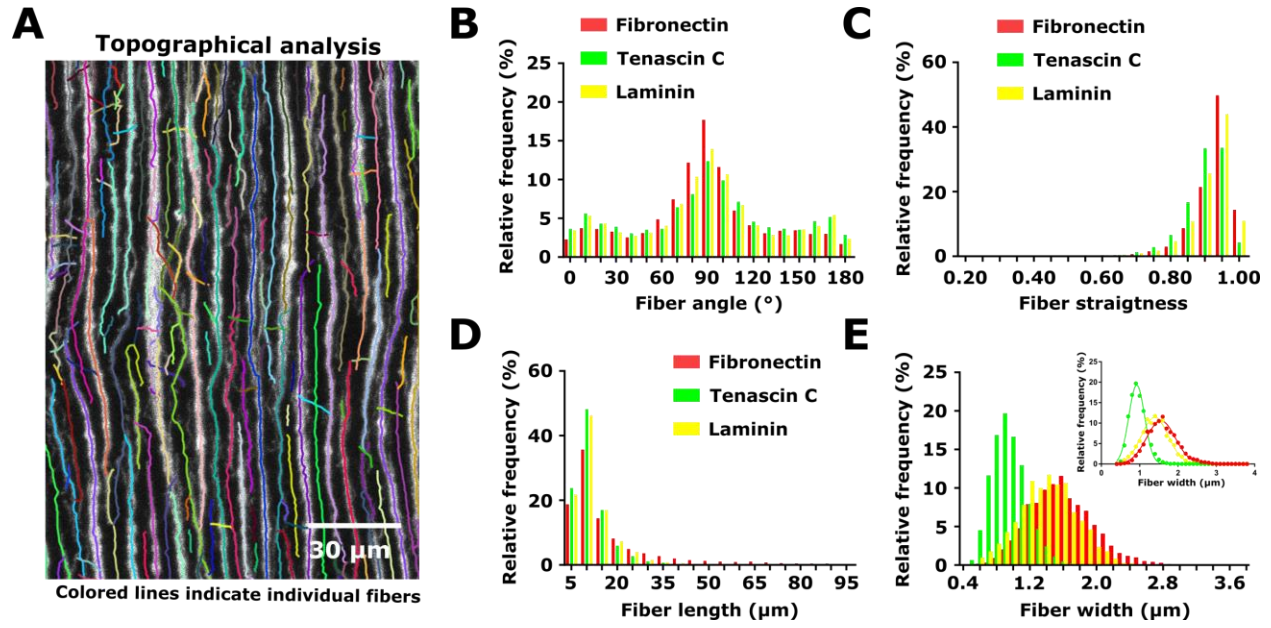
- 1077 [56] Park J, Kim HN, Kim DH, Levchenko A, Suh KY. Quantitative analysis of the combined effect of
1078 substrate rigidity and topographic guidance on cell morphology. *IEEE Trans Nanobioscience*. 2012;11:28-
1079 36.
- 1080 [57] Dalby MJ, Gadegaard N, Tare R, Andar A, Riehle MO, Herzyk P, et al. The control of human
1081 mesenchymal cell differentiation using nanoscale symmetry and disorder. *Nat Mater*. 2007;6:997-1003.
- 1082 [58] Tabdanov ED, Puram VV, Win Z, Alamgir A, Alford PW, Provenzano PP. Bimodal sensing of guidance
1083 cues in mechanically distinct microenvironments. *Nature communications*. 2018;9:4891.
- 1084 [59] Charrier EE, Pogoda K, Wells RG, Janmey PA. Control of cell morphology and differentiation by
1085 substrates with independently tunable elasticity and viscous dissipation. *Nature communications*.
1086 2018;9:449.
- 1087 [60] Huang FK, Han S, Xing B, Huang J, Liu B, Bordeleau F, et al. Targeted inhibition of fascin function blocks
1088 tumour invasion and metastatic colonization. *Nat Commun*. 2015;6:7465.
- 1089 [61] Brownfield DG, Venugopalan G, Lo A, Mori H, Tanner K, Fletcher DA, et al. Patterned collagen fibers
1090 orient branching mammary epithelium through distinct signaling modules. *Curr Biol*. 2013;23:703-9.
- 1091 [62] Conklin MW, Eickhoff JC, Riching KM, Pehlke CA, Eliceiri KW, Provenzano PP, et al. Aligned collagen is
1092 a prognostic signature for survival in human breast carcinoma. *The American journal of pathology*.
1093 2011;178:1221-32.
- 1094 [63] Vicente-Manzanares M, Ma X, Adelstein RS, Horwitz AR. Non-muscle myosin II takes centre stage in
1095 cell adhesion and migration. *Nat Rev Mol Cell Biol*. 2009;10:778-90.
- 1096 [64] Kim D-H, Provenzano PP, Smith CL, Levchenko A. Matrix nanotopography as a regulator of cell
1097 function. *The Journal of Cell Biology*. 2012;197:351-60.
- 1098 [65] Fischer RS, Gardel M, Ma X, Adelstein R, Waterman CM. Myosin II mediates local cortical tension to
1099 guide endothelial cell branching morphogenesis and migration in 3D. *Current biology : CB*. 2009;19:260-
1100 5.
- 1101 [66] Beadle C, Assanah MC, Monzo P, Vallee R, Rosenfeld SS, Canoll P. The role of myosin II in glioma
1102 invasion of the brain. *Mol Biol Cell*. 2008;19:3357-68.
- 1103 [67] Friedl P, Alexander S. Cancer invasion and the microenvironment: plasticity and reciprocity. *Cell*.
1104 2011;147:992-1009.
- 1105 [68] Carbonell WS, Ansorge O, Sibson N, Muschel R. The vascular basement membrane as "soil" in brain
1106 metastasis. *PLoS One*. 2009;4:e5857.
- 1107 [69] Kienast Y, von Baumgarten L, Fuhrmann M, Klinkert WE, Goldbrunner R, Herms J, et al. Real-time
1108 imaging reveals the single steps of brain metastasis formation. *Nat Med*. 2010;16:116-22.
- 1109 [70] Farin A, Suzuki SO, Weiker M, Goldman JE, Bruce JN, Canoll P. Transplanted glioma cells migrate and
1110 proliferate on host brain vasculature: a dynamic analysis. *Glia*. 2006;53:799-808.
- 1111 [71] Oosterhof N, Boddeke E, van Ham TJ. Immune cell dynamics in the CNS: Learning from the zebrafish.
1112 *Glia*. 2015;63:719-35.
- 1113
- 1114

1115 FIGURES



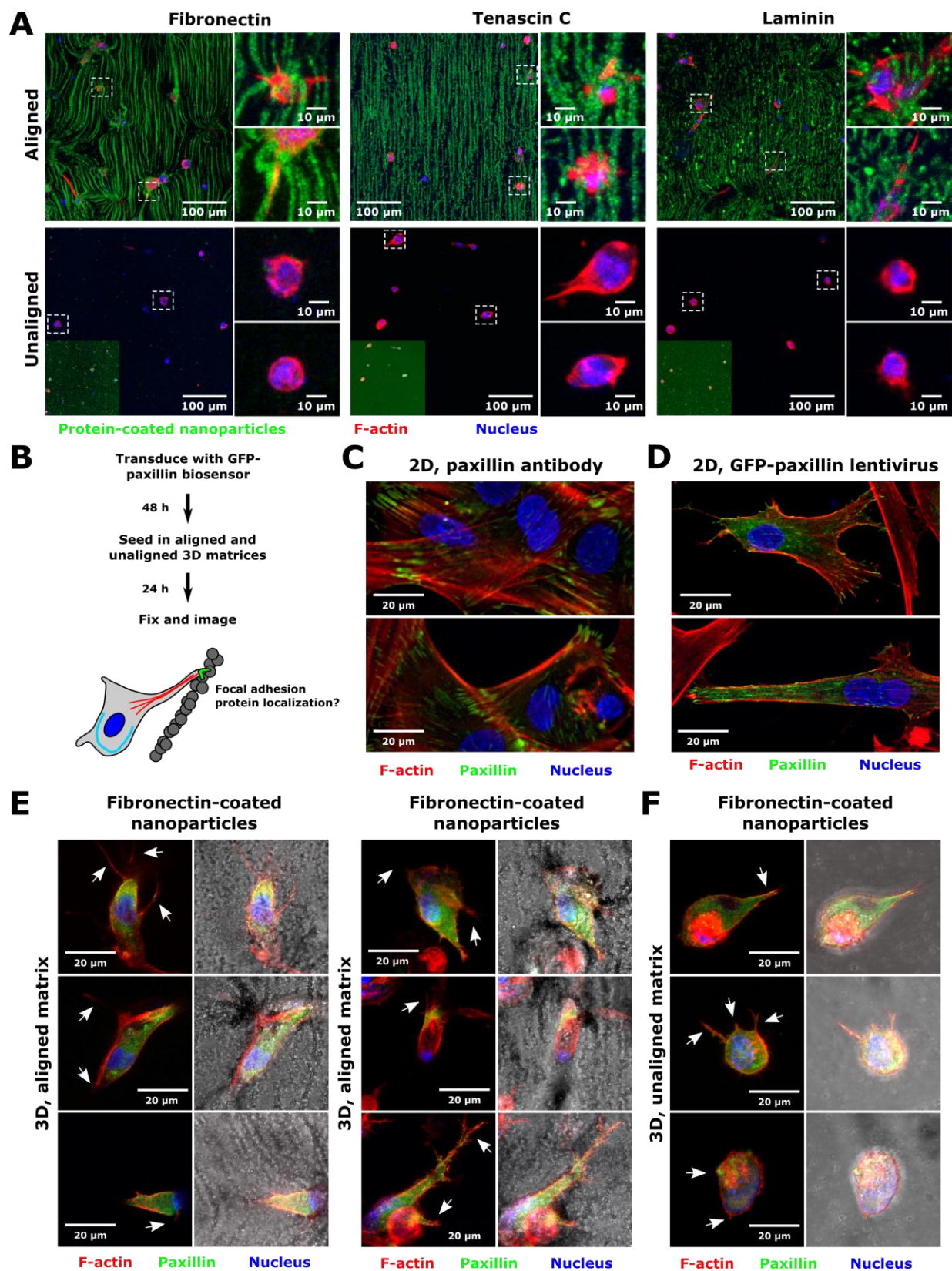
1116

1117 Figure 1



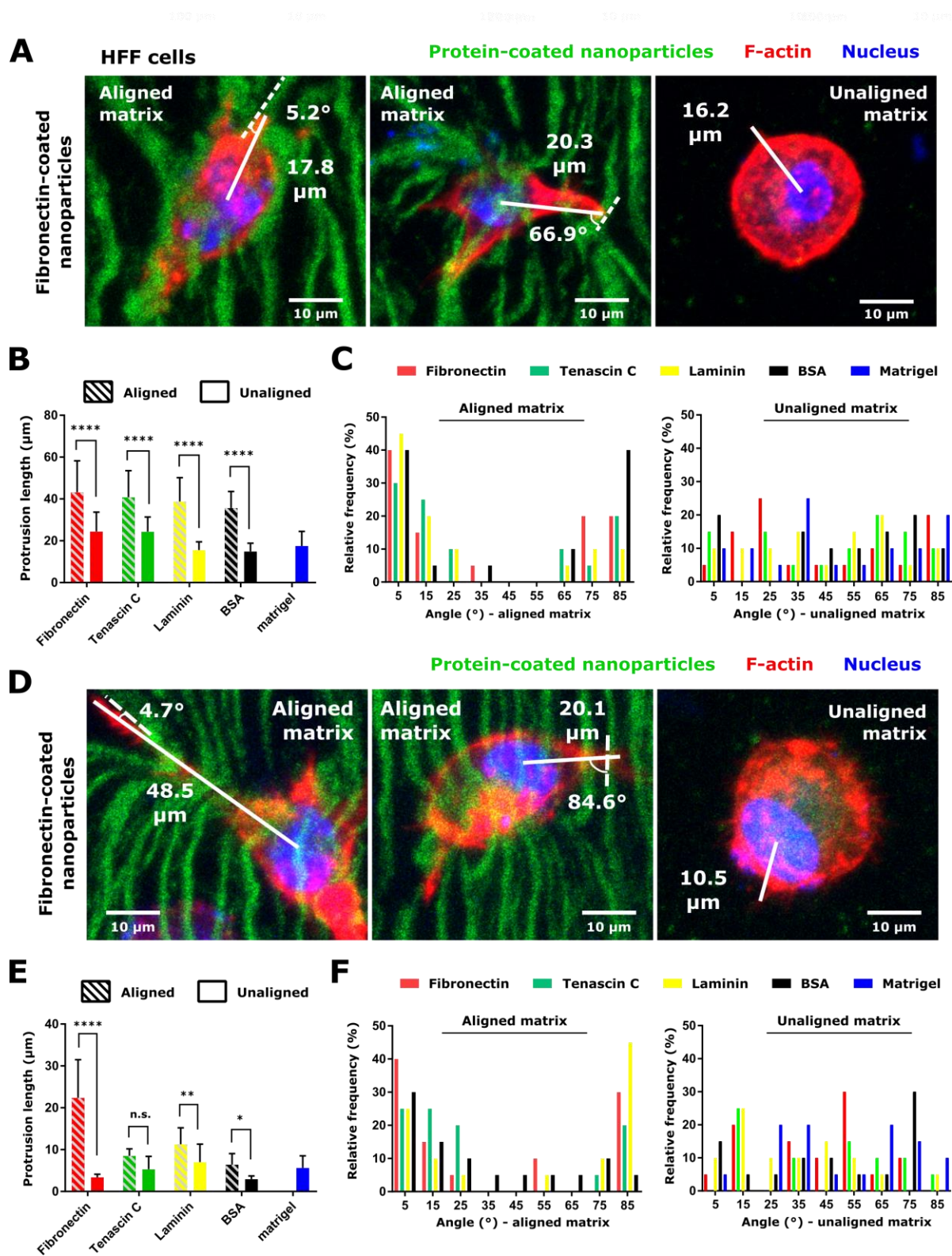
1118

1119 **Figure 2**



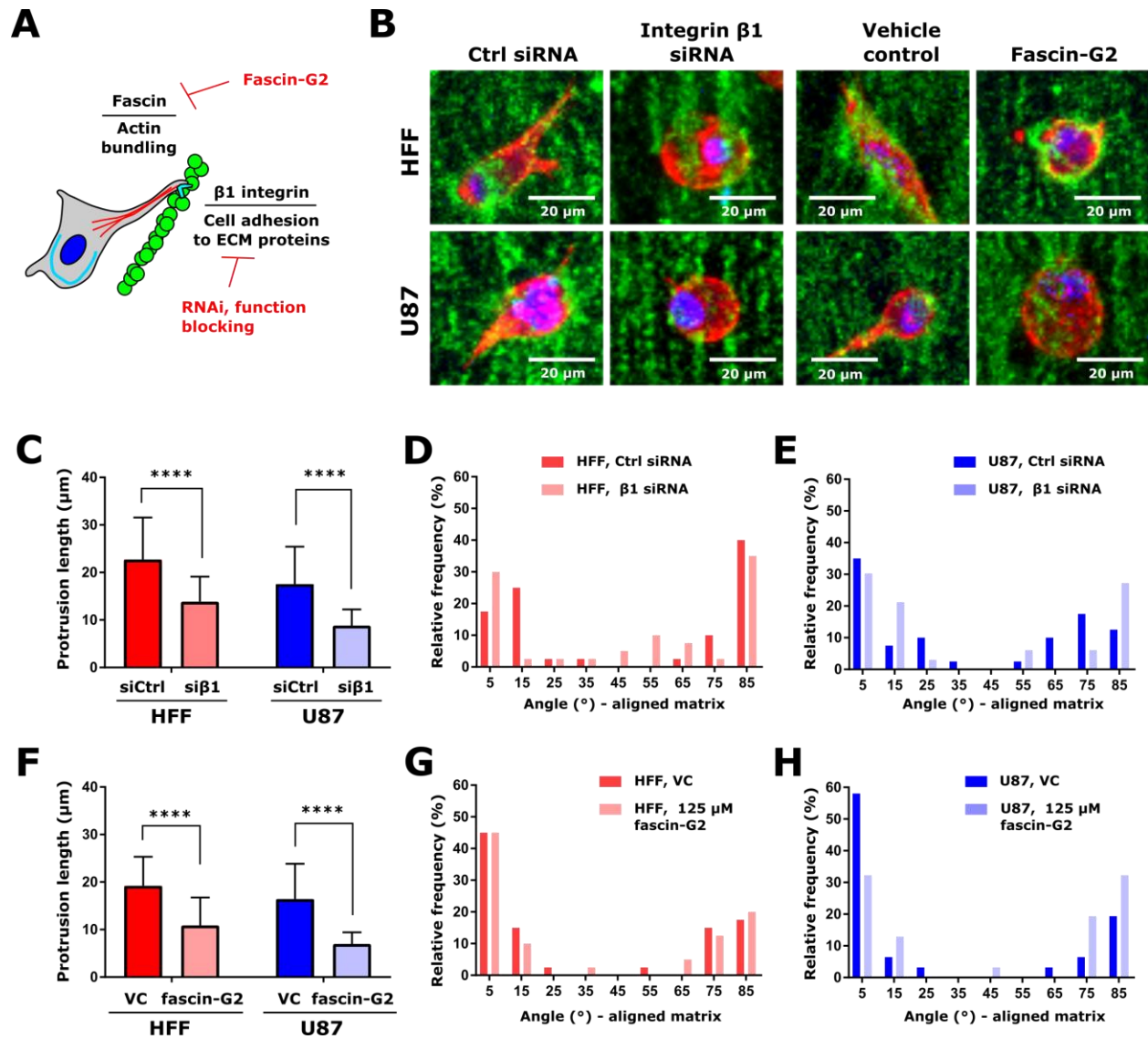
1120

1121 **Figure 3**



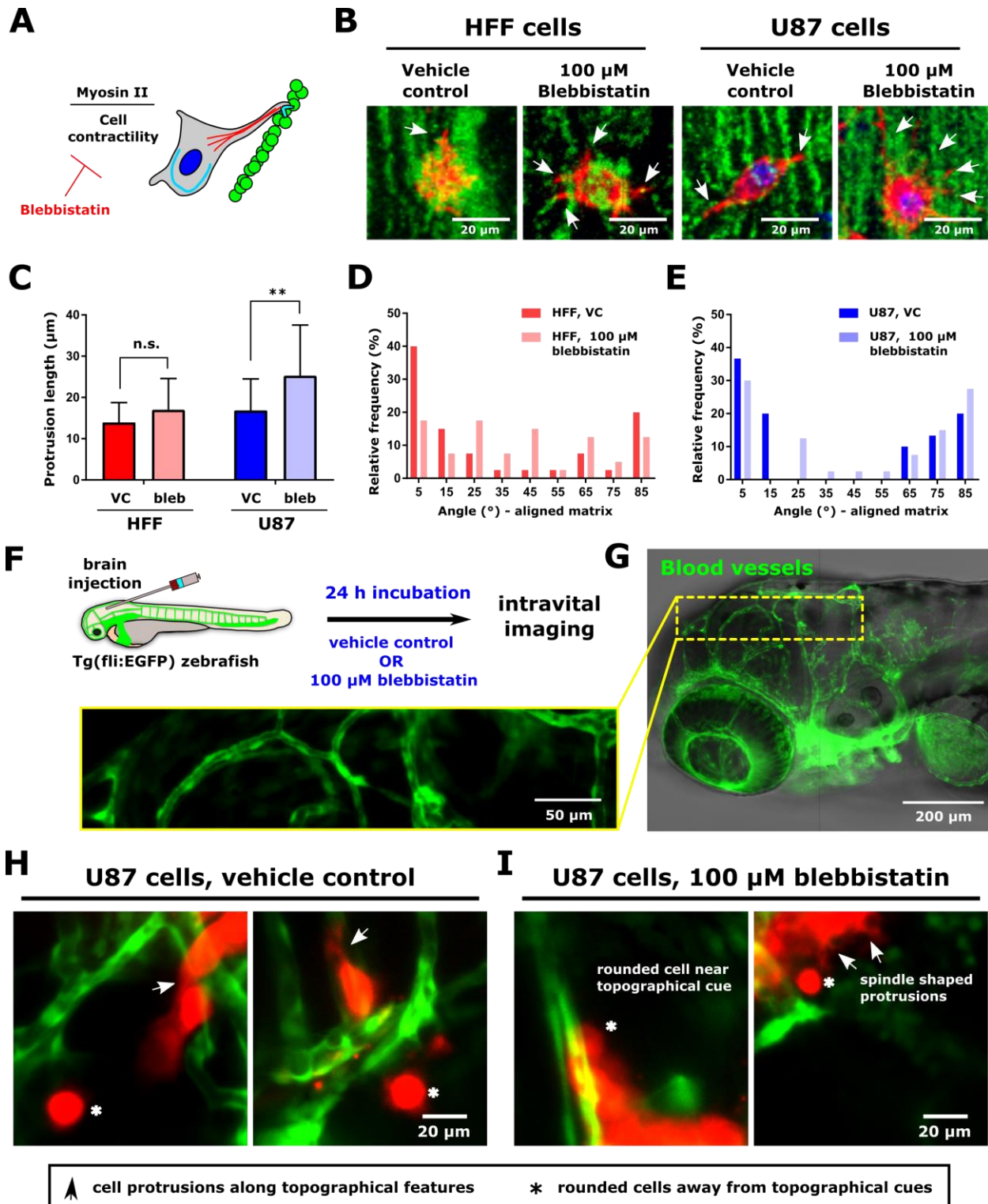
1122

1123 **Figure 4**



1124

1125 **Figure 5**



1126

1127 **Figure 6**

1128

1129 **FIGURE CAPTIONS**

1130

1131 **Figure 1. Characterization of the mechanical properties of engineered matrices across**
1132 **different length scales.** (A) Schematic of 3D matrix patterning process. Human cells and
1133 superparamagnetic colloidal particles were suspended in Matrigel, plated on a glass slide
1134 containing a base layer of Matrigel, and either aligned in a magnetic field (aligned gels) or left
1135 unaligned and dispersed throughout the matrix (unaligned gels). Gels were then formed by
1136 heating at 37°C to set the matrix topography. Cells were fixed for analysis 24 h after seeding. (B)
1137 Complex modulus G^* (mean \pm SEM) vs. frequency curves obtained using optical trap-based
1138 microrheology in gels made with colloidal particles conjugated to human fibronectin. Moduli
1139 were measured at beads in unaligned gels (black), or in aligned gels at distances of 1 μm (blue),
1140 2 μm (green), 3 μm (red), or 4 μm (pink) away from the nearest fiber. Samples were measured in
1141 triplicate, with at least 30 beads per sample analyzed. (C) Schematic and summary of
1142 microrheology experiments. In aligned gels, local stiffness increased closer to the fibers. In
1143 unaligned gels, stiffness was the same throughout the gel. Trend is evident by plotting the
1144 complex modulus (mean \pm standard deviation), normalized to the complex modulus in unaligned
1145 gels, as a function of distance from the nearest fiber. The percentage was averaged across all
1146 measured frequencies for a given fiber distance to obtain the mean and standard deviation. (C)
1147 Bulk elastic (G' , circles) and viscous (G'' , triangles) components of complex moduli (mean \pm
1148 SEM) of Matrigel gels made with colloidal particles coated in human fibronectin (red), tenascin
1149 C (green), or BSA (black), either unaligned (dark red, green, and black) or aligned (light red,
1150 green, and black) within a Matrigel matrix. Measurements were by parallel plate small angle
1151 oscillatory shear (SAOS) bulk rheology and were carried out in duplicate. (E) Elastic (G' ,

1152 squares) and viscous (G'' , triangles) components (mean \pm SEM) of complex moduli of gels
1153 made with colloidal particles conjugated to human fibronectin. Moduli were measured using
1154 either bulk rheology (dark green, dark red) or optical trap-based microrheology (light green, light
1155 red). For microrheology measurements, the moduli values at all distances from the nearest fiber
1156 were combined. Bulk rheology measurements were made in duplicate. For all microrheology
1157 measurements, samples were measured in triplicate, with at least 30 beads per sample analyzed.

1158

1159 **Figure 2. Characterization of the topographical properties of engineered matrices.** (A)
1160 Representative image of fibers formed of fibronectin-conjugated colloidal particles and segmented
1161 using the ctFire fiber analysis toolbox. Colored lines indicate individual fibers segmented for
1162 analysis of fiber morphology. (B) Distribution of fiber angles of to the vertical in Matrigel matrices
1163 containing aligned fibers formed of fibronectin-, tenascin C-, or laminin-conjugated colloidal
1164 particles. (C) Distribution of fiber straightness values in Matrigel matrices containing aligned
1165 fibers formed of fibronectin-, tenascin C-, or laminin-conjugated colloidal particles. (D)
1166 Distribution of fiber lengths in Matrigel matrices containing aligned fibers formed of fibronectin-
1167 , tenascin C-, or laminin-conjugated colloidal particles. (E) Distribution of fiber widths in Matrigel
1168 matrices containing aligned fibers formed of fibronectin-, tenascin C-, or laminin-conjugated
1169 colloidal particles. Inset shows Gaussian fit of fiber width distributions. Three images from the
1170 same matrix were analyzed for aligned fibronectin-conjugated colloidal particles, whereas one
1171 image per matrix were analyzed for matrices containing aligned tenascin C- and laminin-
1172 conjugated colloidal particles. This resulted in analysis of 7288 fibers for fibronectin-conjugated
1173 particles, 4571 fibers for tenascin C-conjugated particles, and 3895 fibers for laminin-conjugated
1174 particles. Colored lines indicate individual fibers segmented for analysis of fiber morphology.

1175

1176 **Figure 3. Human foreskin fibroblast (HFF) cell morphology in a 3D fibrillar matrix system.**

1177 (A) Representative images of HFF cells embedded in aligned or unaligned Matrigel matrices
1178 containing colloidal particles conjugated to fibronectin, tenascin C, or laminin. In each panel,
1179 overview images are shown, with boxes to show detailed cell morphology (cell position in larger
1180 image indicated by dashed white boxes). In unaligned matrix images, insets show unaligned matrix
1181 with lookup table adjusted to show presence of dispersed fluorescent particles. Scales are
1182 indicated. (B) Schematic of experiment to assess focal adhesion protein localization in 3D
1183 matrices. Cells were transduced with a GFP-paxillin lentiviral biosensor prior to being embedded
1184 in aligned and unaligned Matrigel matrices. Cells were fixed, stained, and imaged after being
1185 embedded in matrices for 24 h. (C) Representative images of HFF cell focal adhesion formation
1186 after plating on two-dimensional tissue culture plastic, as assessed by immunofluorescent staining
1187 using a paxillin primary antibody. Images are single confocal slices. F-actin is displayed in red,
1188 paxillin in green, and the nucleus in blue. Scale is indicated. (D) Representative images of HFF
1189 cell focal adhesion formation after plating on two-dimensional surfaces coated with Matrigel, as
1190 assessed using the GFP-paxillin biosensor. Images are maximum intensity projections of confocal
1191 slices. F-actin is displayed in red, paxillin in green, and the nucleus in blue. Scale is indicated. (E)
1192 Representative images of HFF cells in aligned Matrigel matrices containing fibronectin-
1193 conjugated nanoparticles and expressing a GFP-paxillin biosensor. (F) Representative images of
1194 HFF cells in unaligned Matrigel matrices containing fibronectin-conjugated nanoparticles and
1195 expressing a GFP-paxillin biosensor. In panels (E,F), images are maximum intensity projections
1196 of confocal slices containing colloidal particles. F-actin is displayed in red, paxillin in green, and

1197 the nucleus in blue. Brightfield images are shown to illustrate particle alignment. Arrows indicate
1198 cell protrusions in the plane of the fibers. Scale is indicated.

1199

1200 **Figure 4. Increased cell protrusion generation and preferential protrusion orientation in**

1201 **aligned vs. unaligned matrices for HFF and U87 cells.** (A) Representative images of HFF cells

1202 embedded in an aligned and unaligned Matrigel matrix containing colloidal particles conjugated

1203 to fibronectin. Images show detailed morphology of cells with measured protrusion lengths and

1204 protrusion angles. (B) Protrusion length (mean \pm standard deviation) of HFF cells as a function of

1205 matrix alignment status and colloidal particle ECM protein conjugation. Average protrusion length

1206 in Matrigel lacking colloidal particles is also shown. ****, $p < 0.0001$ by Sidak's multiple

1207 comparisons test following two-way ANOVA. (C) Relative frequency distribution of the angle

1208 between HFF protrusions and nearest neighbor fibers (left panel) and in unaligned matrices (right

1209 panel) for Matrigel matrices containing colloidal particles conjugated to human fibronectin,

1210 tenascin C, laminin, or BSA. Protrusion direction distribution in Matrigel lacking colloidal

1211 particles is also shown. For each cell type, matrix alignment status, and nanoparticle ECM protein,

1212 20 protrusions were measured from a single 3D matrix. (D) Representative images of U87 cells

1213 embedded in an aligned and unaligned Matrigel matrix containing colloidal particles conjugated

1214 to fibronectin. Images show detailed morphology of cells with measured protrusion lengths and

1215 protrusion angles. (E) Protrusion length (mean \pm standard deviation) of U87 cells as a function of

1216 matrix alignment status and nanoparticle ECM protein conjugation. Average protrusion length in

1217 Matrigel lacking colloidal particles is also shown. *, $p < 0.05$; **, $p < 0.01$; and ****, $p < 0.0001$ by

1218 Sidak's multiple comparisons test following two-way ANOVA. (F) Relative frequency

1219 distribution of the angle between U87 protrusions and nearest neighbor fibers (left panel) and in

1220 unaligned Matrigel matrices (right panel) for matrices containing colloidal particles conjugated to
1221 human fibronectin, tenascin C, laminin, or BSA. Protrusion direction distribution in Matrigel
1222 lacking colloidal particles is also shown. For each cell type, matrix alignment status, and
1223 nanoparticle ECM protein, 20 protrusions were measured from a single 3D matrix. In panels (A,D),
1224 colloidal particles are displayed in green, F-actin in red, and the nucleus in blue. Images are
1225 maximum intensity projections of confocal slices containing aligned fibers, or of cells embedded
1226 in 3D. Scales are indicated.

1227

1228 **Figure 5. Modulation of protrusion generation via inhibition integrin β 1 activity and actin**
1229 **bundling.** (A) Schematic of cellular processes tested for effect on protrusion generation. Integrin
1230 adhesions were mediated via knockdown of integrin β 1 and application of a function-blocking
1231 antibody, and actin bundling via fascin was inhibited by treatment with the fascin inhibitor fascin-
1232 G2. (B) Representative images of HFF and U87 cells in Matrigel matrices containing aligned
1233 fibronectin-containing particles upon knockdown of integrin β 1 and application of 125 μ M fascin-
1234 G2, or the appropriate controls. Particles are displayed in green, F-actin is displayed in red, and
1235 the nucleus is displayed in blue. Scale is indicated. (C) Cell protrusion length (mean \pm standard
1236 deviation) in cells transfected with siRNA targeting integrin β 1 (si β 1) or non-targeting control
1237 siRNA (siCtrl). (D) Distribution of angles between cell protrusions and the nearest fiber for HFF
1238 cells transfected with siRNA targeting integrin β 1 or non-targeting control siRNA. (E) Distribution
1239 of angles between cell protrusions and the nearest fiber for U87 cells transfected with siRNA
1240 targeting integrin β 1 or non-targeting control siRNA. In panels C-E, two matrices were analyzed
1241 per cell type and treatment. This resulted in analysis of 40 protrusions per condition for HFF cells
1242 and 40 (Ctrl siRNA) or 33 (integrin β 1 siRNA) protrusions analyzed for U87 cells. (F) Cell

1243 protrusion length (mean \pm standard deviation) in cells treated with 125 μ M fascin-G2 or VC. (J)
1244 Distribution of angles between cell protrusions and the nearest fiber for HFF cells treated with 125
1245 μ M fascin-G2 or VC. (G) Distribution of angles between cell protrusions and the nearest fiber for
1246 U87 cells treated with 125 μ M fascin-G2 or VC. In panels (F-H), 20 protrusions were analyzed
1247 from two matrices per cell type and treatment, resulting in 40 protrusions per condition measured.
1248 In panels (C,F), protrusion length was analyzed by Kruskal-Wallis test with Dunn's multiple
1249 comparisons test within each cell type. ****, $p < 0.0001$.

1250

1251 **Figure 6. Modulation of protrusion alignment via inhibition of cell contractility in vitro and**
1252 **in vivo.** (A) Schematic of contractility inhibition experiments. Myosin II-mediated cell
1253 contractility was inhibited with Blebbistatin. (B) Representative images of HFF and U87 cells in
1254 Matrigel matrices containing aligned fibronectin-containing particles upon treatment with 100 μ M
1255 Blebbistatin or vehicle control (VC; DMSO). Arrows indicate cell protrusions. Particles are
1256 displayed in green, F-actin is displayed in red, and the nucleus is displayed in blue. Scale is
1257 indicated. (C) Cell protrusion length (mean \pm standard deviation) in cells treated with 100 μ M
1258 Blebbistatin or VC. (D) Distribution of angles between cell protrusions and the nearest fiber for
1259 HFF cells treated with 100 μ M Blebbistatin or VC. (E) Distribution of angles between cell
1260 protrusions and the nearest fiber for U87 cells treated with 100 μ M Blebbistatin or VC. In panels
1261 (C-E), either two matrices were analyzed per cell type and treatment. This resulted in analysis of
1262 40 protrusions per condition for HFF cells and 30 (VC) or 40 (100 μ M Blebbistatin) protrusions
1263 analyzed for U87 cells. (F) Schematic of in vivo experimental design. Cells were injected to the
1264 hindbrain of transgenic Tg(fli:EGFP) zebrafish, in which vascular epithelial cells express EGFP.
1265 After 24 h incubation fish water supplemented with 100 μ M blebbistatin or VC, cells were imaged.

1266 (G) Overview image of zebrafish brain. Inset shows higher resolution of vessels in the brain.
1267 Vessels are displayed in green. Scale is indicated. (H) Images of U87 cells in the zebrafish brain
1268 following incubation in water supplemented with vehicle control. (I) Images of U87 cells in the
1269 zebrafish brain following incubation in water supplemented with 100 μ M blebbistatin prior to
1270 imaging. Images are average intensity projections of confocal z stacks. Cells are displayed in red,
1271 and zebrafish blood vessels in red. Arrows indicate cell protrusions, while asterisks indicate
1272 rounded cells.

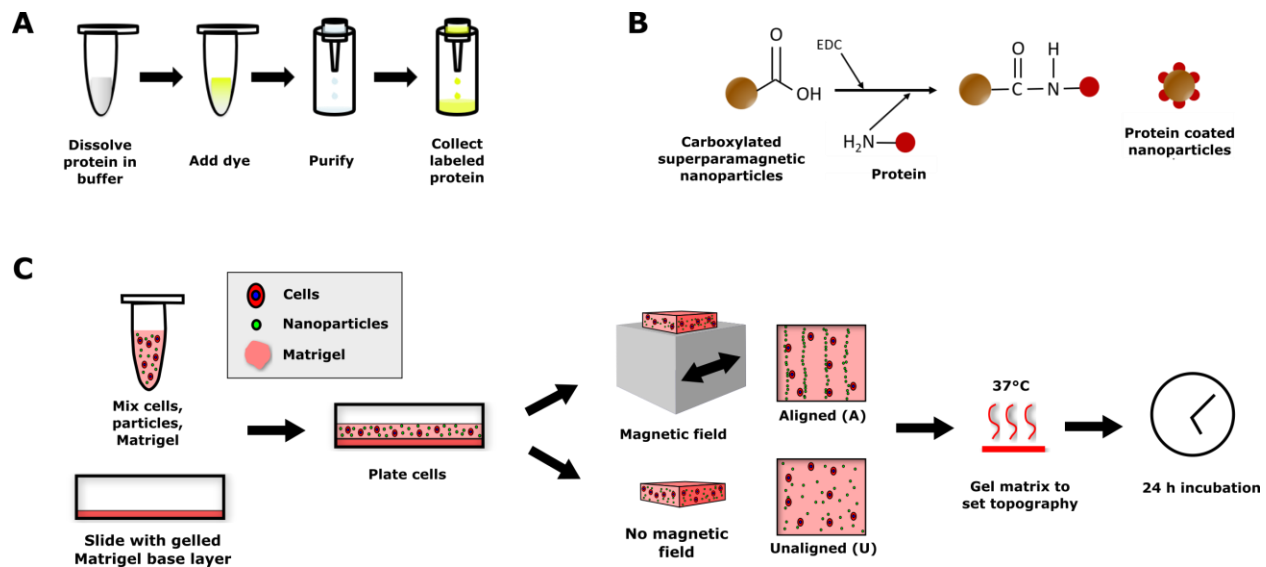
1273

1274

1275 **SUPPLEMENTARY DATA**

1276

1277



1278

1279 **Supplementary Figure 1. Detail of composite hydrogel fabrication process.** (A) Schematic of

1280 procedure used to fluorescently label human extracellular matrix proteins. (B) Schematic

1281 representation of reaction scheme to conjugate human proteins with carboxylated

1282 superparamagnetic magnetic colloidal particles. (C) Schematic of 3D matrix assembly process.

1283 Human cells and superparamagnetic colloidal particles were suspended in Matrigel, plated on a

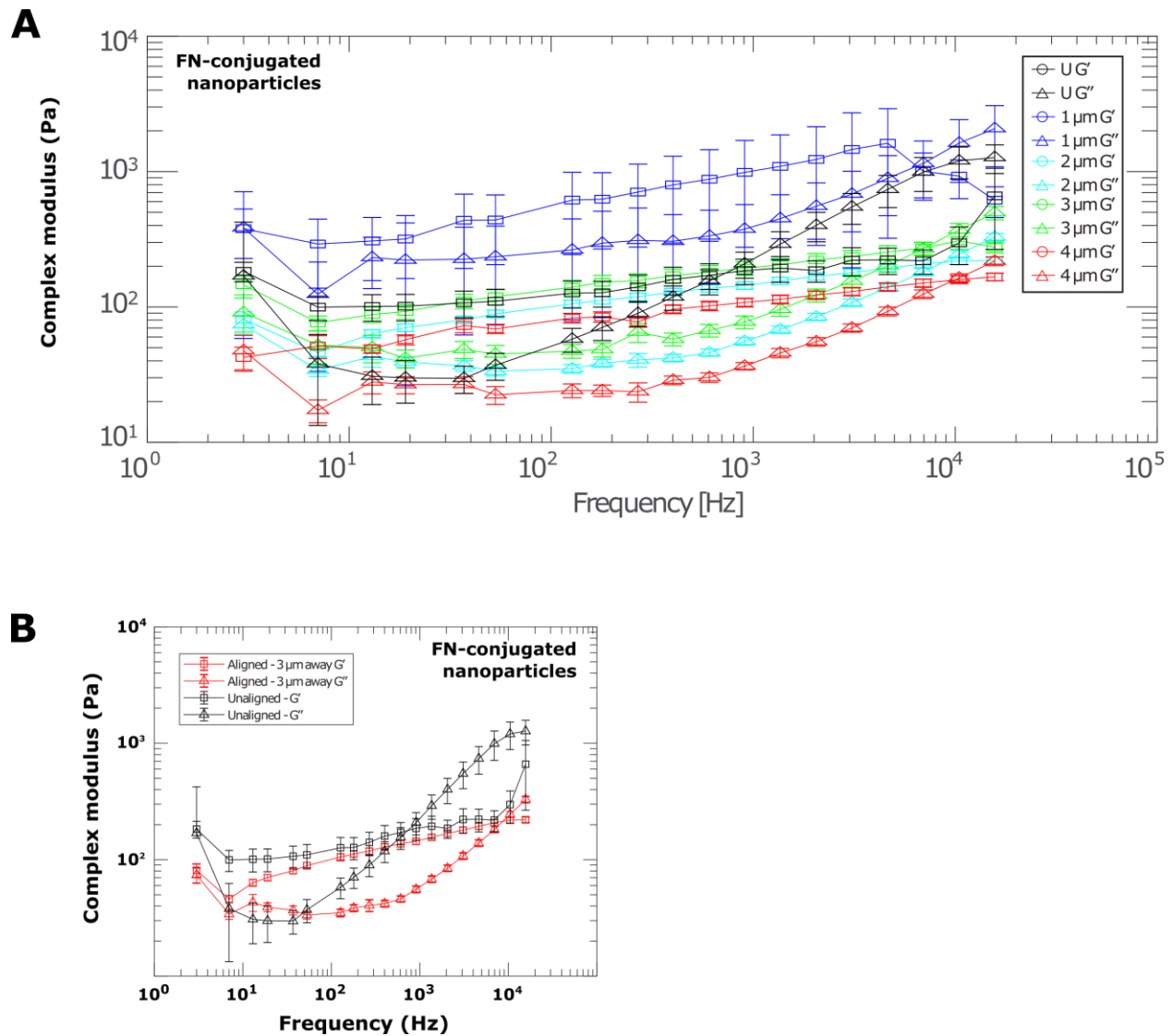
1284 glass slide containing a base layer of Matrigel, and either aligned in a magnetic field or left

1285 unaligned and dispersed throughout the matrix. Gels were then formed by heating at 37°C to set

1286 the matrix topography. Cells were fixed for analysis 24 h after seeding. Portions of this panel are

1287 repeated from Figure 1A to illustrate the entire matrix preparation process.

1288



1289

1290 **Supplementary Figure 2. Frequency dependence of elastic and viscous components of**

1291 **complex modulus of aligned and unaligned gels via active microrheology.** (A) Elastic (G' ,

1292 **circles) and viscous (G'' , triangles) components (mean \pm SEM) of complex moduli of gels made**

1293 **with colloidal particles conjugated to human fibronectin. Moduli measured at beads in unaligned**

1294 **gels (black), or in aligned gels at distances of 1 μm (blue), 2 μm (cyan), 3 μm (green), or 4 μm**

1295 **(red) away from the nearest fiber. (B) Elastic (G' , squares) and viscous (G'' , triangles) components**

1296 **(mean \pm SEM) of complex moduli of gels made with colloidal particles conjugated to human**

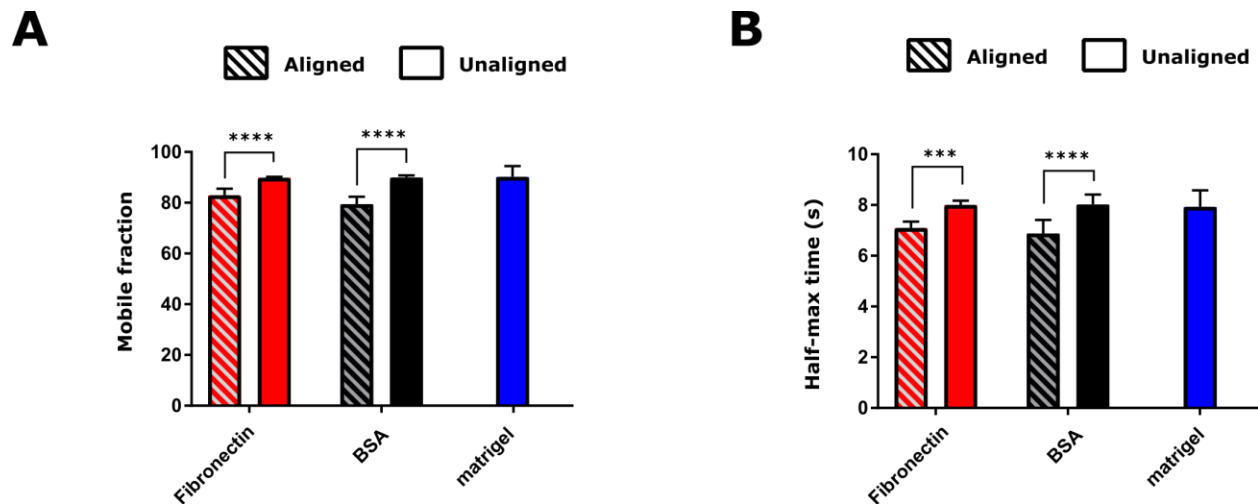
1297 **fibronectin. Moduli measured at beads in unaligned gels (black), or in aligned gels at distances of**

1298 3 μm away from the nearest fiber (red). Data is replotted from Supplementary Figure 2A for clarity.

1299 For all microrheology measurements, samples were measured in triplicate, with at least 30 beads

1300 per sample analyzed.

1301



1302

1303 **Supplementary Figure 3. Fluorescence recovery after photobleaching in aligned and**

1304 **unaligned Matrigel matrices.** (A) Mobile fraction and (B) half-maximum time in aligned and

1305 unaligned Matrigel matrices containing colloidal particles conjugated to fibronectin or BSA, or in

1306 Matrigel matrices without added particles, from fluorescence recovery after photobleaching

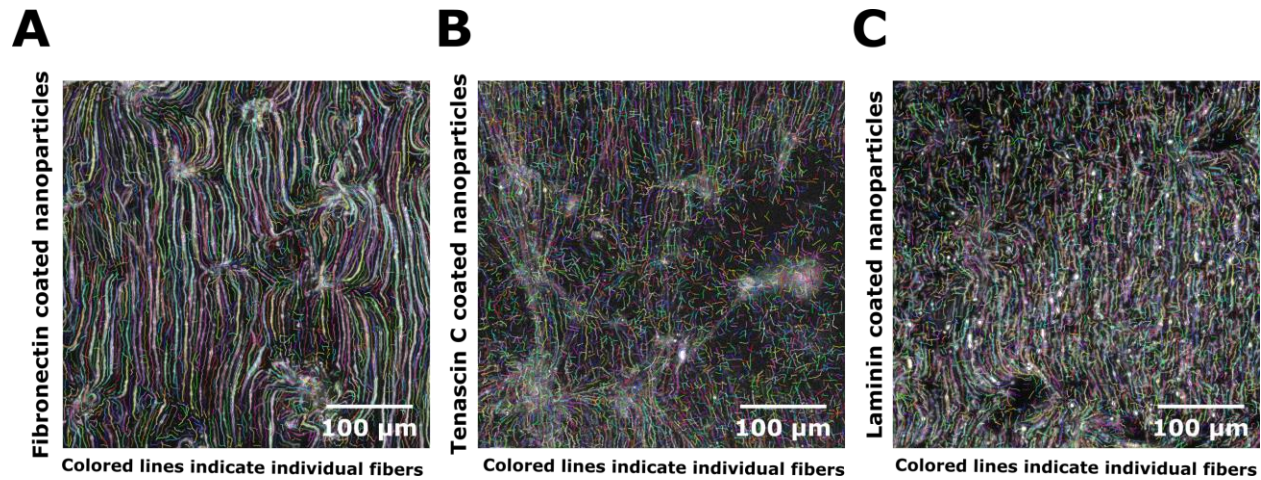
1307 experiments. For each condition (particle protein coating and alignment status), three independent

1308 regions from two gels were measured. These measurements were grouped to obtain N=6 values

1309 prior to statistical comparisons. ***, $p < 0.01$ and ****, $p < 0.0001$ by Sidak's multiple comparisons

1310 test following two-way ANOVA.

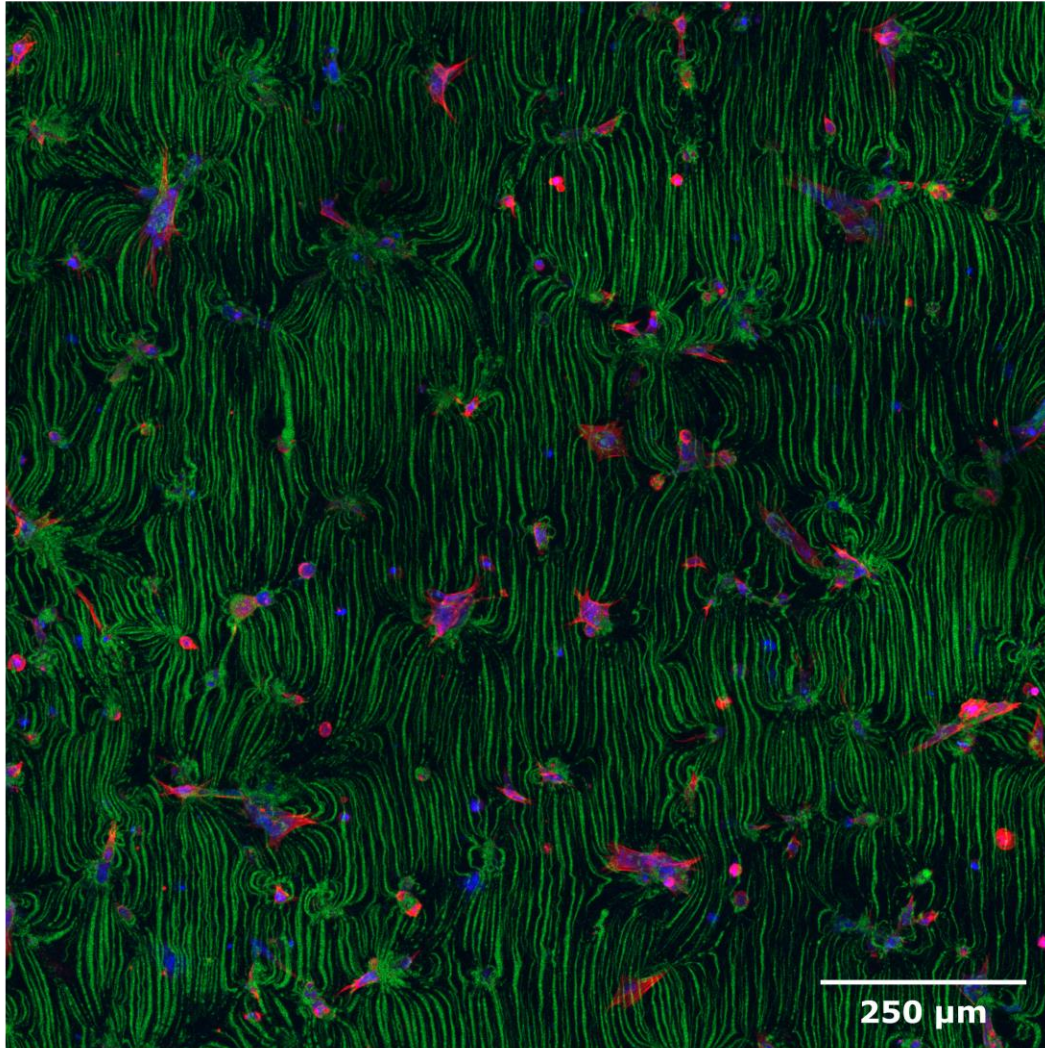
1311



1312

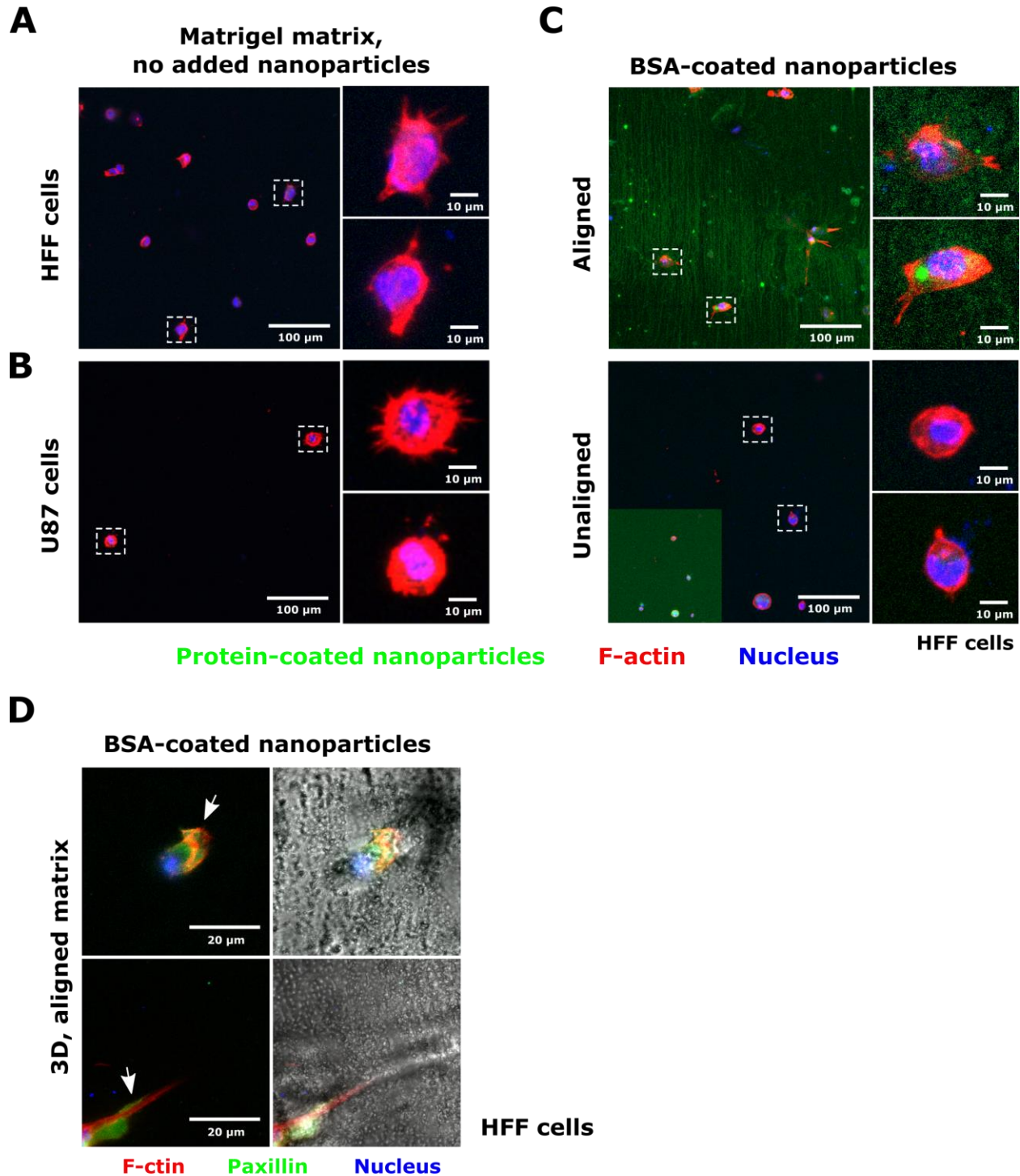
1313 **Supplementary Figure 4. Analysis of fiber properties in aligned matrices containing protein-**
1314 **conjugated colloidal particles.** Representative images of fibers formed of (A) fibronectin-
1315 conjugated colloidal particles, (B) tenascin C-conjugated colloidal particles, and (C) laminin-
1316 conjugated colloidal particles following segmentation using the ctFire fiber analysis toolbox.

A Aligned fibronectin matrix



1317 **Protein-coated nanoparticles** **F-actin** **Nucleus**

1318 **Supplementary Figure 5. Large area, field-based fiber patterning.** Representative images of
1319 HFF cells seeded in an aligned matrix with fibronectin-coated colloidal particles. Using the
1320 magnetic-field based alignment technique, large areas ($>1 \text{ mm}^2$) can be rapidly patterned around
1321 cells embedded in 3D matrices. Colloidal particles are displayed in green, F-actin in red, and the
1322 nucleus in blue. Image is maximum intensity projection of confocal tile scan slices. Scale bar =
1323 250 μm.



1324

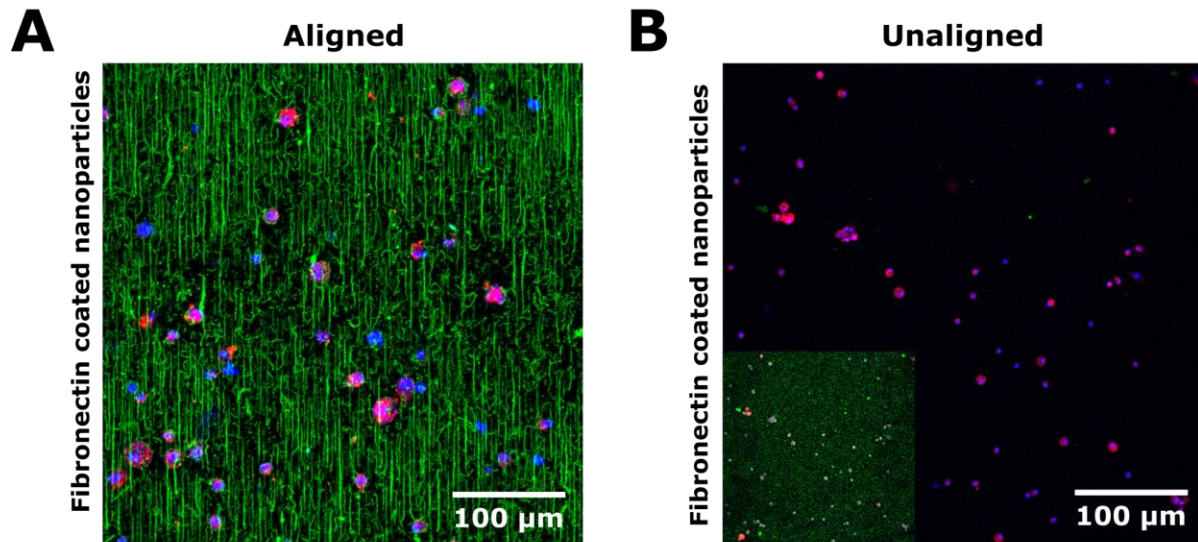
1325 **Supplementary Figure 6. Cell morphology in Matrigel matrices without added colloidal**

1326 **particles and in gels containing BSA-conjugated colloidal particles. Representation images of**

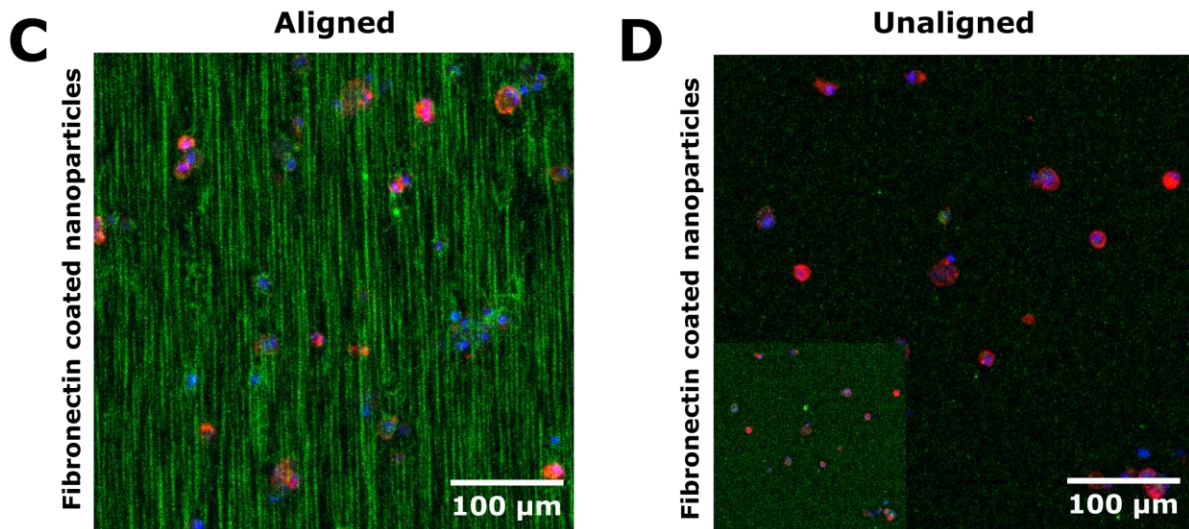
1327 **(A) HFF and (B) U87 cells dispersed in a 3D Matrigel matrix no added Magnetic colloidal**

1328 particles. (C) Representative images of HFF cells embedded in aligned and unaligned matrices
1329 containing colloidal particles conjugated to bovine serum albumin (BSA). Inset in panel C shows
1330 unaligned matrix with lookup table adjusted to show presence of dispersed fluorescent particles.
1331 Magnetic colloidal particles are displayed in green, F-actin is displayed in red, and the nucleus is
1332 displayed in blue. In each panel, overview images are shown, with insets to show detailed cell
1333 morphology (cell position in larger image indicated by dashed white boxes). Images are maximum
1334 intensity projections of confocal slices containing aligned fibers, or of cells embedded in 3D.
1335 Scales are indicated in each image. (D) Representative images of HFF cells in aligned Matrigel
1336 matrices containing BSA-conjugated nanoparticles and expressing a GFP-paxillin biosensor.
1337 Images are maximum intensity projections of confocal slices containing colloidal particles. F-actin
1338 is displayed in red, paxillin in green, and the nucleus in blue. Brightfield images are shown to
1339 illustrate particle alignment. Arrows indicate cell protrusions in the plane of the fibers. Scale is
1340 indicated.

Hyaluronic acid matrix



Agarose matrix

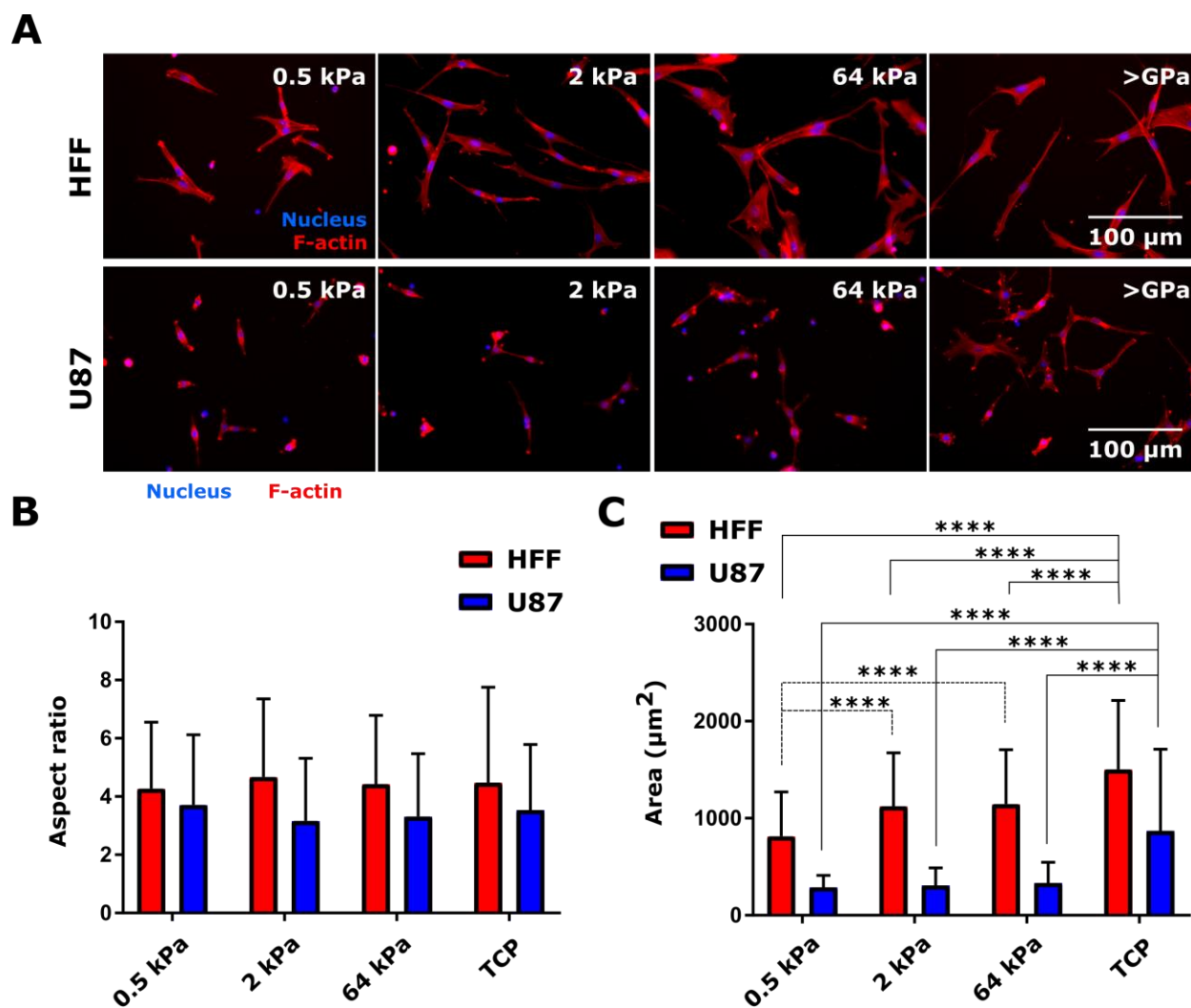


1341

1342 **Supplementary Figure 7. Engineered fibers in multiple 3D cell culture matrices.** Human
1343 foreskin fibroblasts were embedded in hyaluronic acid matrices containing (A) aligned or (B)
1344 unaligned fibronectin-conjugated colloidal particles, or agarose matrices containing (C) aligned or
1345 (D) unaligned fibronectin-conjugated colloidal particles. Insets in unaligned matrix examples
1346 show the same unaligned matrix image with lookup table adjusted to show presence of dispersed

1347 fluorescent particles. Colloid particles are displayed in green, F-actin in red, and the nucleus in
1348 blue. Images are maximum intensity projections of confocal slices containing aligned fibers.
1349 Scales are indicated.

1350



1351

1352 **Supplementary Figure 8. Effect of substrate stiffness on HFF and U87 cell morphology.** (A)

1353 Representative fluorescence images of HFF and U87 cells seeded on silicone substrates with

1354 elastic modulus of 0.5, 2, or 64 kPa, or on tissue culture plastic (TCP, >GPa stiffness). Surfaces

1355 were coated with 1 $\mu\text{g}/\text{ml}$ human fibronectin. F-actin is displayed in red, and the nucleus in blue.

1356 Scale is shown. (B) Aspect ratio (mean \pm standard deviation) and projected cell area (mean \pm

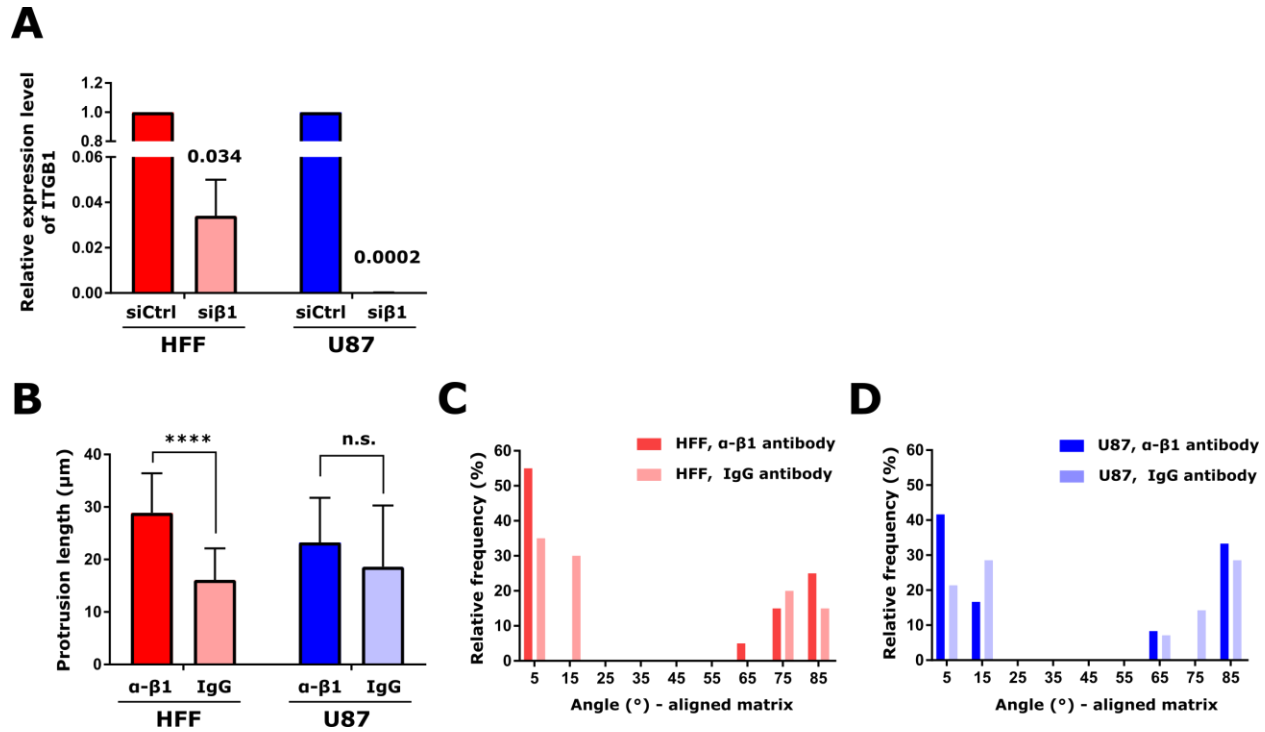
1357 standard deviation) as a function of cell type and substrate stiffness. Area and aspect ratio values

1358 among conditions were compared using two-way ANOVA with Tukey's multiple comparisons

1359 post-test between all combinations of substrate stiffness for a given cell type. ****, $p < 0.0001$.

1360 Measurements were made for two samples per cell type and substrate stiffness, and samples were
1361 prepared simultaneously. At least 73 cells were analyzed for each condition.

1362



1363

1364 **Supplementary Figure 9. Knockdown efficiency and effects of integrin β1 function blocking**

1365 **on cell protrusion and protrusion angles in aligned matrices.** (A) Relative expression of

1366 integrin β1 (ITGB1) in HFF or U87 cells transfected with non-targeting control siRNA or siRNA

1367 directed against integrin β1. Expression was assessed via qPCR with relative expression

1368 calculated from gene $\Delta\Delta cT$. GAPDH was used as the housekeeping gene. Numbers indicate

1369 relative expression upon knockdown. (B) Cell protrusion length (mean \pm standard deviation) in

1370 cells treated with 30 μ g/ml function-blocking antibody against integrin β1 (α -β1) control IgG

1371 antibody (IgG). (C) Distribution of angles between cell protrusions and the nearest fiber for HFF

1372 cells treated with 30 μ g/ml function-blocking antibody against integrin β1 (α -β1) control IgG

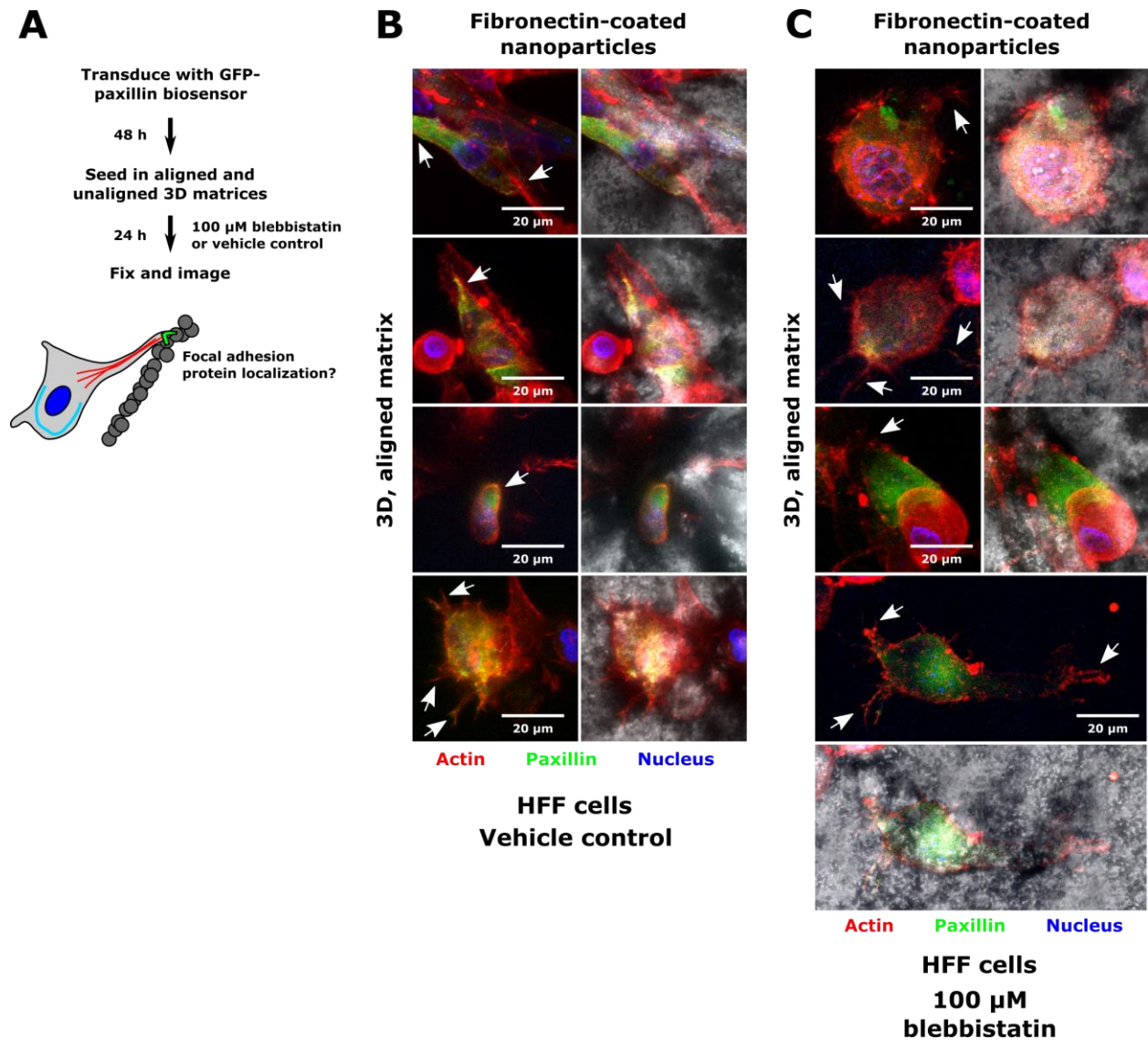
1373 antibody (IgG). (D) Distribution of angles between cell protrusions and the nearest fiber for U87

1374 cells treated with 30 μ g/ml function-blocking antibody against integrin β1 (α -β1) control IgG

1375 antibody (IgG). In panels B-D, one matrix was analyzed per cell type and treatment, with 20

1376 protrusions per condition analyzed for HFF and 12 and 14 protrusions analyzed for U87 α - β 1 and
1377 IgG cells, respectively.

1378

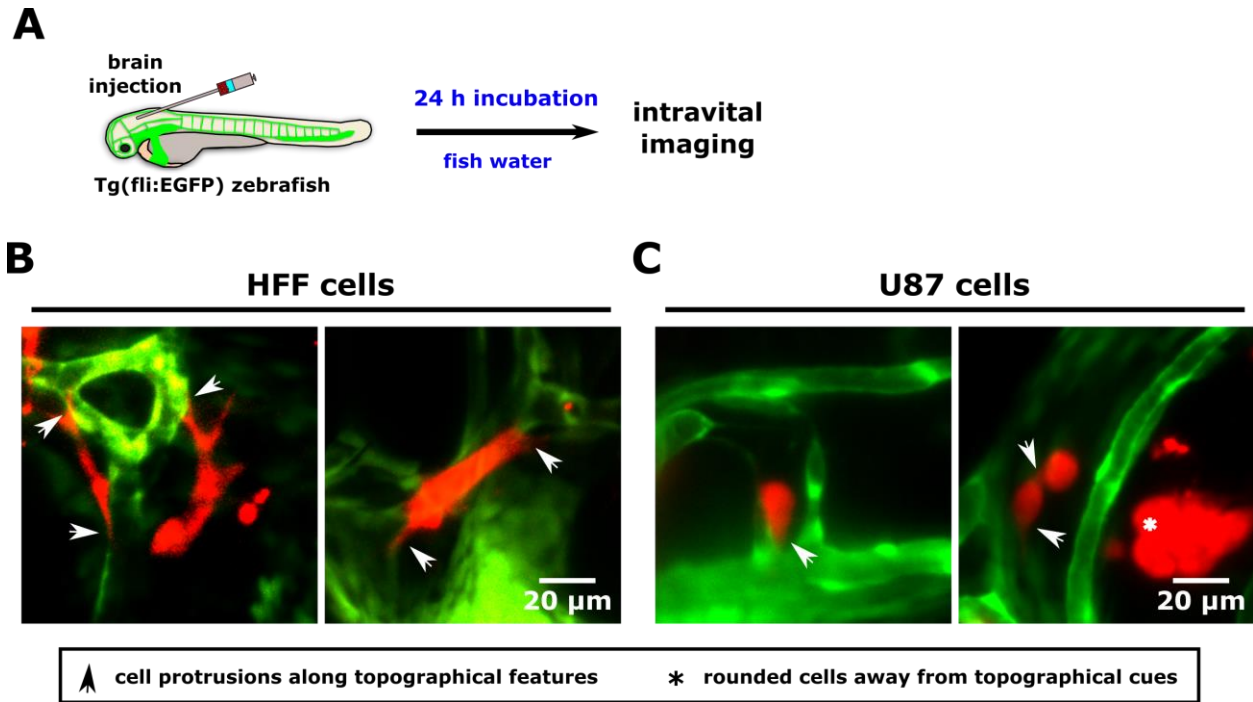


1379

1380 **Supplementary Figure 10. Human foreskin fibroblast (HFF) paxillin expression upon**
1381 **blebbistatin treatment.** (A) Schematic of experiment to assess focal adhesion protein localization
1382 in HFF cells in 3D matrices in the presence of blebbistatin. Cells were transduced with a GFP-
1383 paxillin lentiviral biosensor prior to being embedded in aligned and unaligned Matrigel matrices

1384 in the presence of 100 μ M blebbistatin or vehicle control. Cells were fixed, stained, and imaged
1385 after being embedded in matrices for 24 h. (B) Representative images of HFF cells in aligned
1386 Matrigel matrices containing fibronectin-conjugated nanoparticles and expressing a GFP-paxillin
1387 biosensor in the vehicle control case. (C) Representative images of HFF cells in aligned Matrigel
1388 matrices containing fibronectin-conjugated nanoparticles and expressing a GFP-paxillin biosensor
1389 after treatment overnight with 100 μ M blebbistatin. In panels (B,C), images are maximum intensity
1390 projections of confocal slices containing colloidal particles. F-actin is displayed in red, paxillin in
1391 green, and the nucleus in blue. Brightfield images are shown to illustrate particle alignment.
1392 Arrows indicate cell protrusions in the plane of the fibers. Scale is indicated.

1393



1394

1395 **Supplementary Figure 11. Alignment of cells to topographical cues in the in vivo zebrafish**

1396 **brain microenvironment.** (A) Schematic of experimental design. Cells were injected to the

1397 hindbrain of transgenic Tg(fli:EGFP) zebrafish, in which vascular epithelial cells express EGFP.

1398 After 24 h incubation in fish water, cells were imaged. (B) Images of HFF cells in the zebrafish

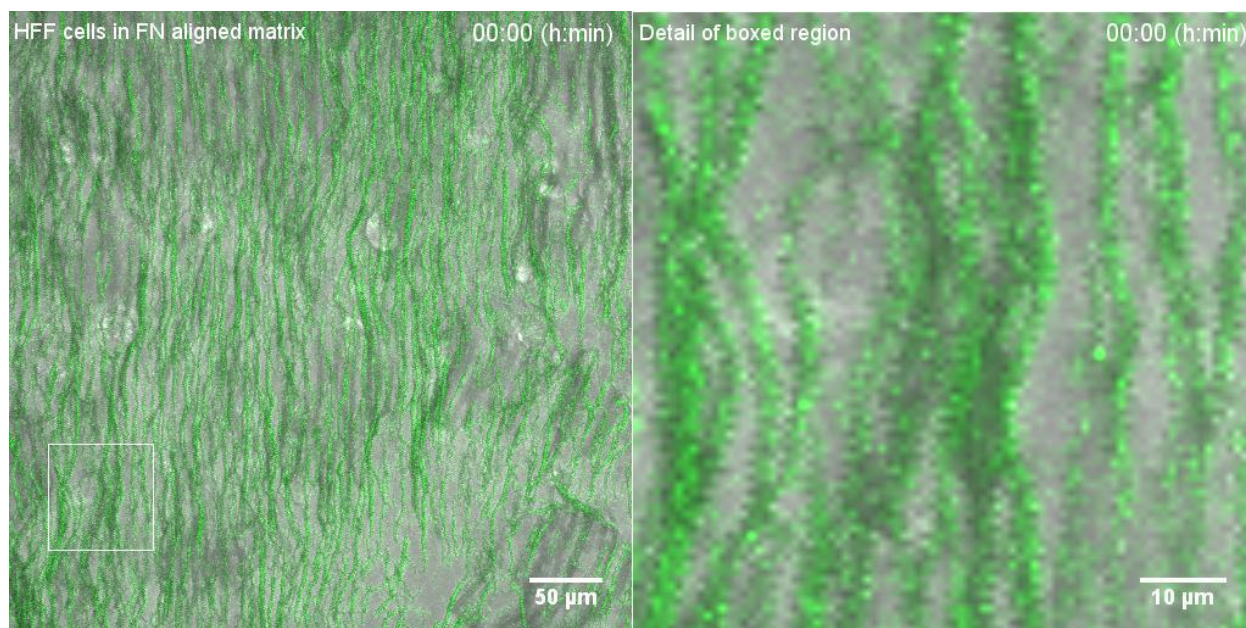
1399 brain following incubation in fish water. (C) Images of U87 cells in the zebrafish brain following

1400 incubation in fish water. Images are average intensity projections of confocal z stacks. Cells are

1401 displayed in red, and zebrafish blood vessels in red. Arrows indicate cell protrusions, while

1402 asterisks indicate rounded cells.

1403



1404

1405 **Supplementary Video 1. Time-lapse video of HFF cell protrusion and contraction in aligned**

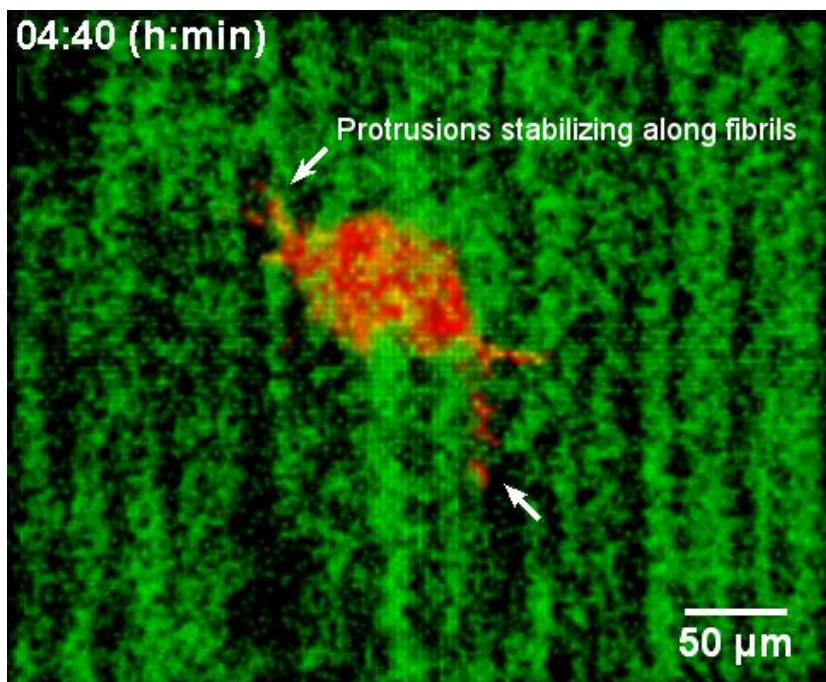
1406 **matrix.** HFF cells (bright field) were plated in aligned matrices containing fibronectin-conjugated

1407 colloidal particles (green). Time-lapse video shows cells protruding in and contracting the matrix.

1408 White box indicates region of interest shown in detail in right panel. Images show maximum

1409 intensity projection of confocal z slices and were acquired every 10 min, starting immediately after

1410 matrix topography was set.



1411

1412 **Supplementary Video 2. U87 cell actin cytoskeletal imaging reveals protrusion maturation**

1413 **along aligned fibers.** A U87 cell was transduced with a LifeAct adenovirus (red) and plated in

1414 an aligned matrix containing fibronectin-conjugated colloidal particles (displayed in green).

1415 Video shows 3D reconstruction of confocal z slices, which were acquired every 10 min. Time

1416 stamps and scale bars are indicated. Arrows point to protrusions forming along fibrils.